Universidad Técnica Federico Santa María
Departamento de Obras Civiles
Santiago - Chile

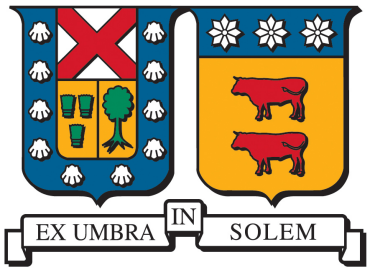

Experimental validation of the performance of the robust adaptive model-based compensator for real-time hybrid simulation

Master's Thesis by
Daniel Maurel Escobedo

Submitted in partial fulfillment of the requirements for the degree of Master of Science in Civil Engineering

Advisor
Gastón Fermadois Cornejo, PhD

Acknowledgments

Abstract

One of the goals of structural engineers is to predict and understand how structures behave and use knowledge to design safer structures and calibrate building codes. Even when the numerical models have improved to a great extent and represent a good estimator of the performance of a structure, they can't reproduce all the possible complex interactions, and they need to be calibrated by real-life observations or laboratory tests, which can be expensive. Real-time hybrid simulation is an experimental technique that allows the mix of numerical and experimental models by using sensors and actuators. The main idea is to experimentally test a component of interest and its interaction with a numerical model that simulates the rest of the structure, making it a reliable and cost-effective technique. However, due to the dynamics between the actuator and the structure, not all signals can be properly controlled over the experimental component, and some errors are introduced. To mitigate these errors, researchers have used dynamic compensators that modify the target signals to overcome the interaction of the actuator with the structure. Classical compensators typically require testing and identifying the dynamics of the experiment, making compensators tailored to the specific parameters of the experiment and, therefore, impractical to perform multiple different experiments. On the other hand, more modern approaches use variable parameters to adapt the compensator to the system, but they can become unstable. The AMBC is an adaptive parameter compensator based on models that include the uncertainty of the parameters to ensure robustness, and it had prove good performance in virtual real-time hybrid simulation. This study describes experimental tests conducted to assess the performance of the adaptive model-based compensator in a real-time hybrid simulation of a three-story structure equipped with a tuned mass damper and compare the results against a traditional feedforward compensator. Results showed that the adaptive model-based compensator outperformed the feedforward compensator in most of the tested scenarios, with average improvements in performance up to 6 ms on average delay, 1.3% on synchronization RMS error, 6% on peak error, and no stability issues.

Keywords: Real time hybrid simulation; dynamic compensation; adaptive model-based compensation; experimental testing.

Contents

List of Figures

List of Tables

Glossary

AMBC Adaptive Model-Based Compensator. II, 4, 35, 37, 44, 51, 52, 53, 54, 57, 58, 59, 61

ATS Adaptive Time Series. 35

BLWN Band Limited White Noise. 30

CATS Conditional Adaptive Time Series. 35

DOF degree of freedom. 12

HS Hybrid Simulation. 2, 6, 7

MAC-KF Model Adaptive Control using Kalman Filter. 35

MPC Model Predictive Control. 35

RMS Root Mean Squared. II, 37

RTHS Real-Time Hybrid Simulation. V, 2, 4, 8, 9, 10, 28, 30, 32, 33, 52, 58, 61

SDOF Single degree of freedom. 12, 13, 17

SO Specific objectives. 3

SSP Subspace synchronization plots. 29, 32

TMD Tuned Mass Damper. V, VI, VII, 4, 12, 13, 14, 16, 17, 18, 19, 20, 21, 22, 23, 30, 39, 42, 43, 51, 55, 58, 61

Chapter 1

Introduction

1.1 Motivation

One of the objectives of structural engineering is to produce safer structures with better serviceability. To accomplish this objective, engineers make predictions of the performance of their designs and compare their results against building codes based on knowledge and experience. These performance predictions are typically based on numerical models representing the structure behavior. Although numerical models have improved considerably in recent years, they still approximate the structures' actual behavior, which introduces uncertainty. To improve their structural reliability it is possible to validate the models by performing experimental tests that recreate the phenomena of interest (Melchers & Beck, 2018). For example, Kaba and Mahin (1984) validated models for reinforced concrete using monotonic, cyclic, and dynamic tests. However, testing large structures at full scale is too expensive or impossible given laboratories' capabilities, especially since the objective is usually to study a specific component's contribution to system-level performance. Hybrid simulation (HS) emerges as an alternative technique to study the behavior of the complete structure without physically building all the structure. HS consists of an experimental technique where the specimen of interest is physically tested in conjunction with a numerical substructure that simulates the rest of the structure. Sensors are used to measure the response of the specimen, and actuators to enforce the boundary conditions imposed by the numerical substructure, and depending on the phenomena of study, the test can be done in a dilated scale of time instead of real-time (Saouma & Sivaselvan, 2008).

Real-time hybrid simulation (RTHS) was born as a solution for systems dependent on velocity or acceleration (Nakashima et al. 1992). RTHS is a hybrid simulation technique where numerical integration, actuator motion, and digital signal processing must be executed in real time (close to milliseconds). However, running the target signals before the next time step can be challenging due to the actuator dynamics, and differences between the commanded and measured signals are usually unavoidable. These differences are typically shown as delay or magnitude errors that must be accommodated for robustness and accuracy purposes. These errors not only affect the accuracy of the test results but can also induce instabilities that cause unwanted damage (Horiuchi, 1996).

Dynamic compensators are proposed to improve synchronization in RTHS experiments, which modify the target signal, taking into account the actuators' dynamics to reduce the error between the target and measured signal. Although various compensators can be found in the literature, this study will review two types: (i) Feedforward and (ii) adaptive model-based compensators. In the case of the feedforward compensator, the compensator is calibrated based on the properties

of the model, which are typically identified from the specimen. However, any error or change in the identified properties translates into a deterioration of the compensator performance and may even generate instability in the system. Another problem is nonlinear behavior because the system's nonlinearity will affect the structure-actuator interaction, and even when the system can be linearized, this is typically only a valid small range of target values, limiting the compensator's operating range. In contrast, adaptive compensators can adapt their parameters during the test. However, they must be designed with knowledge of the control plant and the control-structure interaction, therefore, the compensator is linked to the experiment. Moreover, it is necessary to redesign the compensator in case of changing the control plant, like a change in experiment parameters or significant damage to the specimen. Besides, adaptive compensators must be used with care because they can become unstable if they are too aggressive. Due to these limitations, there is a need for a robust compensator that can adapt and be applicable for multiple control plants without redesigning the compensator, introducing the concept of robust adaptive model-based compensator.

In this study, the implementation and experimental validation of a robust model-based adaptive compensator proposed by Gálmez and Fermandois (2020) is presented. This compensator shows good results in virtual tests, however, it has not been experimentally validated, so there is a gap between the virtual and the actual capabilities of such a compensator. This work corresponds to the last stage of the Fondecyt Iniciación No. 11190774 project "Dynamic compensation of real-time hybrid simulation test for time-varying, nonlinear structural models under seismic loading".

1.2 Objectives

This study aims to experimentally test the performance and robustness of the adaptive model-based compensator on a real-time hybrid simulation. A set of specific objectives (SO) are defined to achieve this goal:

[SO1] Design and manufacture an experimental testbed to perform real-time hybrid simulations in the Dynamics Laboratory of the Civil Engineering Department at Universidad Federico Santa María and validate the results against a reference model.

[SO2] Design and implement the feedforward and adaptive model-based compensator for dSpace hardware.

[SO3] Perform dynamic tests to benchmark the performance of the adaptive model-based compensator against the feedforward compensator.

1.3 Structure of the thesis

The study is divided into four main chapters. First, there is a brief introduction and motivation to study real-time hybrid simulation (RTHS) and the adaptive model-based compensator (AMBC). The second chapter focuses on implementing RTHS for a physical model of a three-story building equipped with a tuned mass damper (TMD) and validating the results compared to a reference model. In the third chapter, the experimental framework is developed to test the performance of the AMBC in multiple scenarios. The results of the AMBC's performance are compared with a more classical approach (feedforward compensator). Finally, the fourth chapter presents the study's conclusions and recommendations for future research.

Chapter 2

Real time hybrid simulation of a building equipped with a tuned mass damper

2.1 Literature review

2.1.1 Hybrid simulation

Hybrid simulation (HS) is an experimental technique that allows subdividing a test into a numerical and an experimental component by using sensors that measure the response of the experimental component, and actuators that prescribe boundary conditions at the interface between numerical and experimental substructures. The main goal of the methodology is to provide a cost-effective, reliable test that experimentally tests the components with uncertain behavior in a numerical framework that represents a more realistic condition than pushover or cyclic tests. For example, a new dampening device (experimental component) can be tested like it is installed on a structure (numerical component) subjected to a seismic loading instead of being tested in an incremental cyclic load pattern.

HS had its beginnings in the work developed by Hakuno et al. (1969) in which a cantilevered steel beam subjected to an arbitrary load was studied (Figure 2.1). On one side, the dynamics associated with the inertial and dampening are solved numerically. Conversely, the displacements obtained from the numerical model are imposed on the physical specimen to obtain the nonlinear restitutive force.

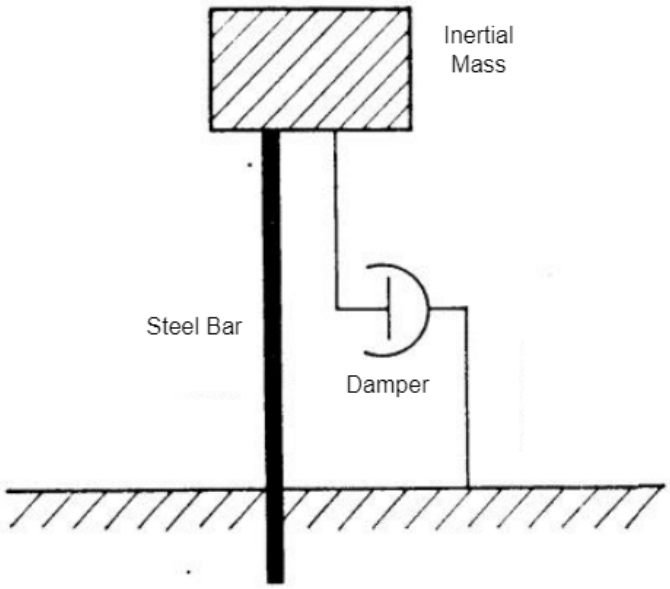

Figure 2.1: Diagram of the system tested by Hakuno et al. (1969)

Later, Takanashi et al. (1975) performed similar tests but using a digital computer and formally

coined the term pseudo-dynamic test. Finally, the concept of substructuring was introduced by Dermitzakis and Mahin (1985), where the structure is divided into a numerical substructure compatible with an experimental substructure, shaping what we know today as hybrid simulation. A simplified scheme of a hybrid simulation test is shown in Figure 2.2.

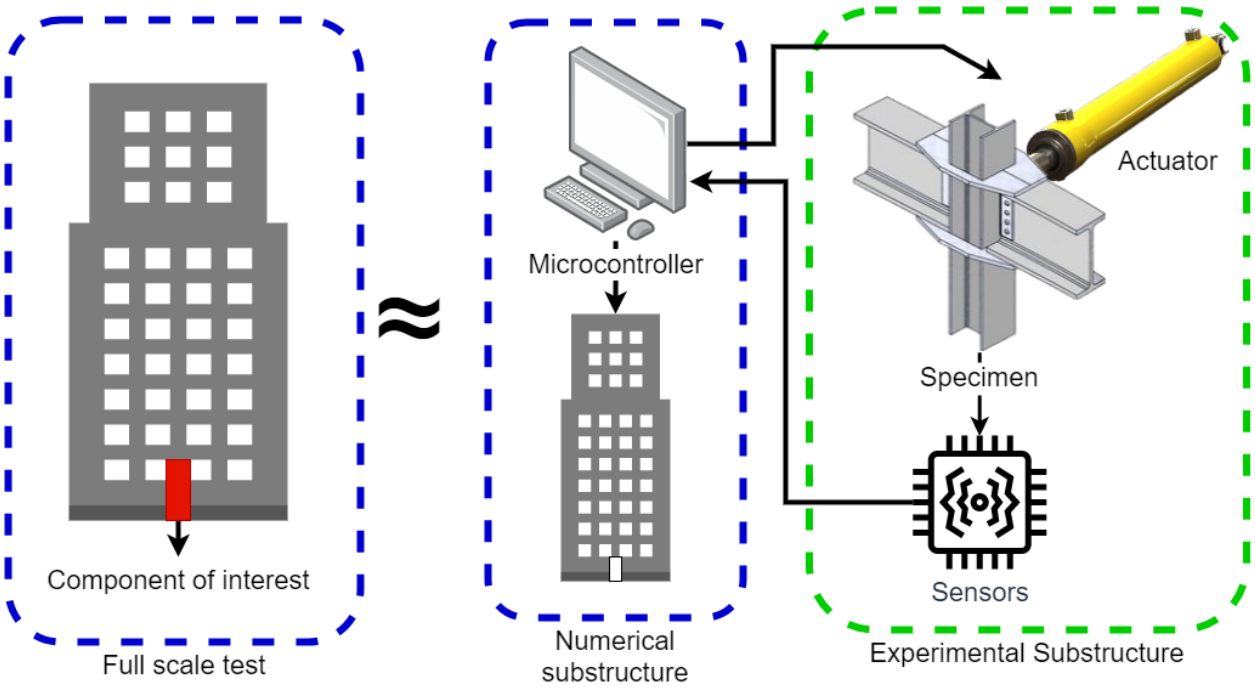

Figure 2.2: Simplified diagram of an hybrid simulation test.

One of the benefits of HS is that it allows the study of components of interest without the need to fabricate the entire structure in the laboratory, significantly reducing the costs associated with the construction of the specimen and the capacity of the facilities but maintaining a high level of test reliability. On the other hand, if the phenomenon to be analyzed does not depend on velocity or acceleration, it is possible to perform the test on a dilated time scale, allowing the actuators sufficient time to achieve the target position, thus reducing the errors between the measured and target signal. For example, in a dilated time-scale experiment, the results of the numerical substructure are imposed on the experimental substructure at a slow rate. When the target is reached, the measured signal is provided to integrate the next time step on the numerical substructure. This process can take several timesteps, and there is no need to impose the boundary conditions or integrate the numerical substructure in a limited execution time, making it easier to test complex numerical substructures or use a broader range of actuators. The downside of this approach is that the duration of the experiment can be increased several times. Besides, in systems dependent on

acceleration or velocity, all actions must be executed before the next timestep.

2.1.2 Real time hybrid simulation

Real-time hybrid simulation (RTHS) arises as an alternative to cases in which there is a time dependence of the specimen behavior. Hence time cannot be scaled, which implies that the boundary conditions imposed by the actuators must be commanded and executed in real-time. It was initially proposed by Nakashima et al. (1992) for a one-degree-of-freedom system with viscous dampers subjected to seismic loading; in this test, the inertial and stiffness components of the equations of motion are solved numerically in a computer, and the velocity-dependent dampening forces are obtained experimentally.

Nakashima et al. (1992) proposed a methodology where a digital microcomputer integrates the equation of motion, and the obtained response is used to impose the displacements of the experimental substructure in 20 [ms] cycles. After, displacement and velocity are sent to a digital servo mechanism that controls the displacement of a dynamic actuator in a closed loop form in cycles of 2 [ms]. Finally, after 20 [ms], the viscous damper force obtained from a load cell is reported to the microcontroller, and the next time step is integrated. Figure 2.3 shows a simplified diagram of the experiment.

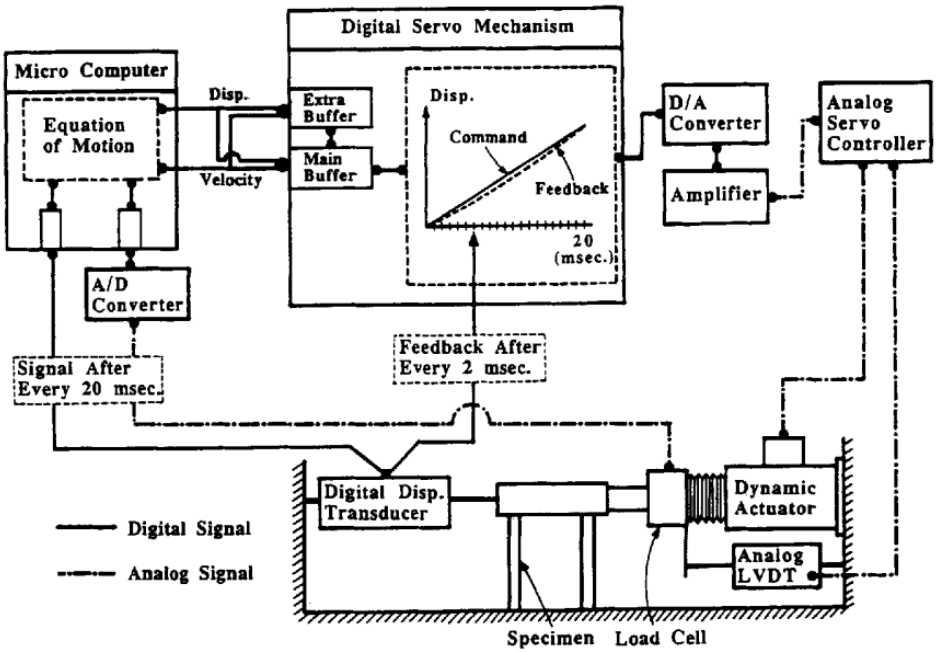

Figure 2.3: Simplified diagram of the pseudo-dynamic test performed by Nakashima. (Nakashima et al. 1992)

Real-time execution poses a significant challenge when testing, as it requires specialized hardware and the ability to numerically integrate the structure in a time step on the order of 1 [ms] (Carrion et al. 2010). This restriction in timestep is mainly because the objective is to enforce a continous-time signal over the specimen using digital computers. Besides, the stability of a digital system relies in part on the timestep size which also limits the timestep size. The timestep must be small enough to avoid instability so the system doesn't have poles with positive real parts. Also, some numerical integration methods are conditionally stable, and their stability depends on the timestep size.

Furthermore, the problem is not only performing the numerical integration in a small timestep but also quickly moving the actuators to the desired position without error. Theoretically, an ideal actuator can instantly move to the desired position; however, real-world actuators have mass, friction, and physical limitations from motors, valves, pumps, or mechanical components. Therefore, they introduce a dynamic system between the actuator and the structure, and they cannot instantly move the experimental substructure to the target. To reduce errors, mechanical systems, hydraulic valves, accumulators, and cylinders must be designed according to the requirements of the experiment. But, these measures cannot solve entirely the issue of actuator dynamics and tracking errors in RTHS testing.

2.1.3 Dynamic compensators

Due to the dynamics between the actuators and the specimen, the measured signal tends to delay behind the commanded signal and overshoot or undershoot (Figure 2.4), which can generate instabilities in the system or invalidate the test results due to large errors. In extreme cases, the commanded signal can be greater than the maximum physical capabilities of the actuators (stroke, fluid velocity, max current, etc.) and end up damaging the specimen and the actuators (Dyke et al. 1995), (Horiuchi et al. 1999). For this reason, it is necessary to use dynamic compensators that modify the commanded signal to mitigate the effects of the actuator-structure dynamics, reducing the amplitude and delay errors. It is also important to notice that if the compensator is poorly designed, it can also generate system instability or inaccurate simulation results.

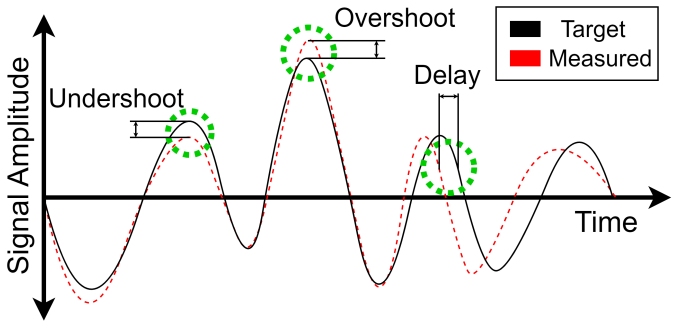

Figure 2.4: Typical errors between the target and measured signals.

The target signal comes as a result of integrating the numerical substructure. Then, the target and measured signals are passed through a dynamic compensator; as a result, the command signal is obtained and sent to the actuators. It should be noted that the target and commanded signals are the same if there is no compensation. Also, a generic scheme is shown in Figure 2.5. In the particular case of this chapter, a feedforward compensator is implemented.

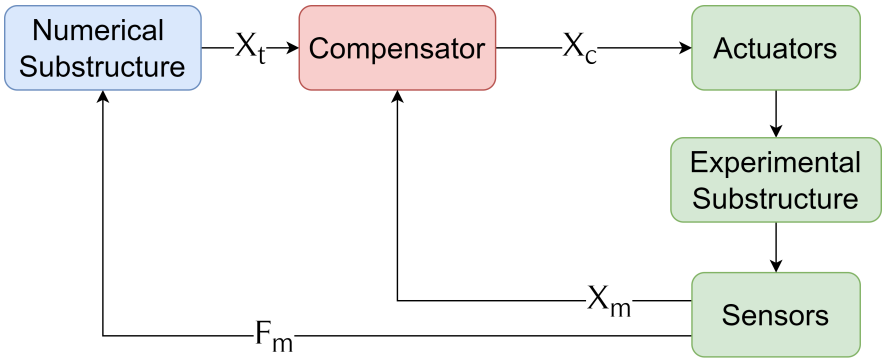

Figure 2.5: Compensation process on a RTHS, X_t is the target signal, X_c is the commanded signal, X_m is the measured signal and F_m is a measured quantity.

The feedforward compensator is a form of open-loop control used to mitigate the actuator-structure dynamics. For this purpose, the feedforward compensator uses the inverse of the transfer function of the experimental actuator-substructure system (Carrion et al. 2007). The main idea behind a feedforward compensator is that the structure-actuator interaction can be modeled as a transfer function from the target signal to the measured signal. So, as the target signal is passed through the inverse of the transfer function of the actuator-structure interaction, the system becomes a unity-gain zero-phase open-loop system. Hence, the target and measured signals are the same due to compensation.

However, to design the feedforward compensator, it is necessary to know the transfer function of

the actuator-structure dynamic, which usually involves identifying the system to be compensated; this implies that the system's transfer function is fixed. The problem with this approach is that the transfer function can vary significantly in the presence of nonlinear behavior, making the compensation sub-optimal or, in extreme cases, introduce instability due to the large gains in feedforward's high frequency range, and the presence of high-frequency noise. Another limitation of this approach is that the inverse of the transfer function of the structure-actuator can be unstable, Figure 2.6 shows an unbounded controller. Nevertheless, an unstable controller can still result in a stable system, which is usually impractical due to plant uncertainty. To avoid unbounded compensators, some authors have added poles to the system so that the order of the transfer function's denominator is larger than the numerator. These poles are usually set to be several times larger than the original compensator poles to not affect the compensator's performance at the frequency range of interest (Carrion et al. 2007). Moreover, Phillips and Spencer (2013) proposed the feedforward feedback compensation where the feeedforward compensator is complemented with a linear quadratic gaussian (LQG) controller to close the control loop. In Phillips and Spencer (2013) approach the problem of an improper controller is addressed using finite differences to estimate high order derivatives and avoid introducing unwanted dynamics to the system (as happens with a low-pass filter). Nevertheless, the use of a low-pass filter is still recommended in cases where the high order derivatives are not available or are inaccurate (Phillips & Spencer, 2013); (Phillips & Spencer, 2011).

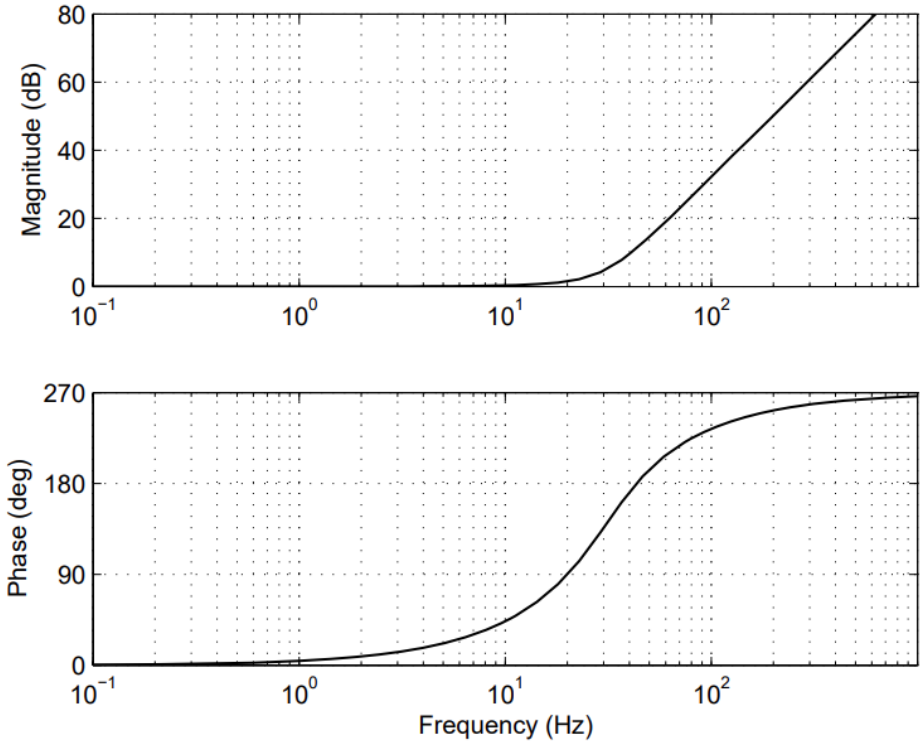

Figure 2.6: Example of a feedforward controller that with large gains in higher frequency. (Carrion et al. 2007)

2.1.4 Tuned mass damper

The tuned mass damper is a device that uses an inertial mass tuned to the fundamental period of the structure in which the interaction of the TMD with the structure reduces the building vibrations (Connor, 2003). The first patented application of the TMD concept was in 1909, where an inertial mass was used to reduce hull vibrations and the rolling motions of ships (Frahm, 1909). However, the theory behind the TMD was formally presented in 1928 for a single degree of freedom (SDOF) system subjected to sinusoidal excitation (Ormondroyd & Den Hartog, 1928). Figure 2.7 shows a single degree of freedom system equipped with a TMD, where k and c are the stiffness and damping parameters of the system; m and m_d are the mass of the system and the TMD; k_d and c_d are the stiffness and damping parameters of the TMD respectively; u is the system degree of freedom (DOF) and u_d is the displacement of the TMD mass relative to the system DOF and P is an external excitation force.

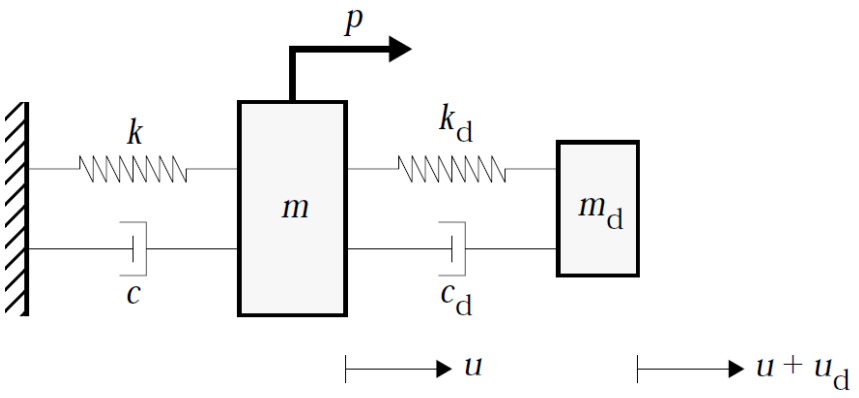

Figure 2.7: Single degree of freedom system equipped with a TMD. (Connor, 2003)

Based on the parameters shown in the Figure 2.7 the equation of motion of the system equipped with the TMD can be defined as:

$$(1+\bar{m})\ddot{u} + 2\xi\omega\dot{u} + \omega^2 u = \frac{p}{m} - \bar{m}\ddot{u}_d \tag{2.1}$$

$$\ddot{u}_d + 2\xi_d\omega_d\dot{u}_d + \omega_d^2 u_d = -\ddot{u} \tag{2.2}$$

where ω, c , w_d, c_d and $\bar{m}$ are defined as:

$$\omega^2 = \frac{k}{m} \tag{2.3}$$

$$c = 2\xi\omega m \tag{2.4}$$

$$\omega_d^2 = \frac{k_d}{m_d} \tag{2.5}$$

$$c_d = 2\xi_d\omega_d m_d \tag{2.6}$$

$$\bar{m} = \frac{m_d}{m} \tag{2.7}$$

$$\tag{2.8}$$

It has been proven that for an SDOF system subjected to periodical excitation, optimal parameters to minimize the amplification factor H_2 (Equation 2.10) can be found (Randall et al. 1981); (Warburton, 1982); (Tsai & Lin, 1993). Furthermore, Figure 2.8 shows that the amplification factor H_2 is minimal when the TMD is set to its optimal damping. On the other hand, Figures 2.9 and 2.10 show that the TMD's optimal damping ratio and frequency depends on the mass ratio between the TMD and the system. The mass ratio also affects the system's minimum response, decreasing as the ratio augments, as shown in Figure 2.11. However, TMDs that are too big may be impractical in real-life applications.

$$|D_2| = \sqrt{\left([1-\rho^2]\,[f^2-\rho^2]-\bar{m}\rho^2 f^2\right)^2+\left(2\xi_d\rho f\,[1-\rho^2(1+\bar{m})]\right)^2} \tag{2.9}$$

$$H_2 = \frac{\sqrt{\left[(1+\bar{m})f^2-\rho^2\right]^2+\left[2\xi_{\mathrm{d}}\rho f(1+\bar{m})\right]^2}}{|D_2|} \tag{2.10}$$

where ρ and f are defined as:

$$\rho = \frac{\Omega}{\omega} \tag{2.11}$$

$$f = \frac{\omega_d}{\omega} \tag{2.12}$$

$$\tag{2.13}$$

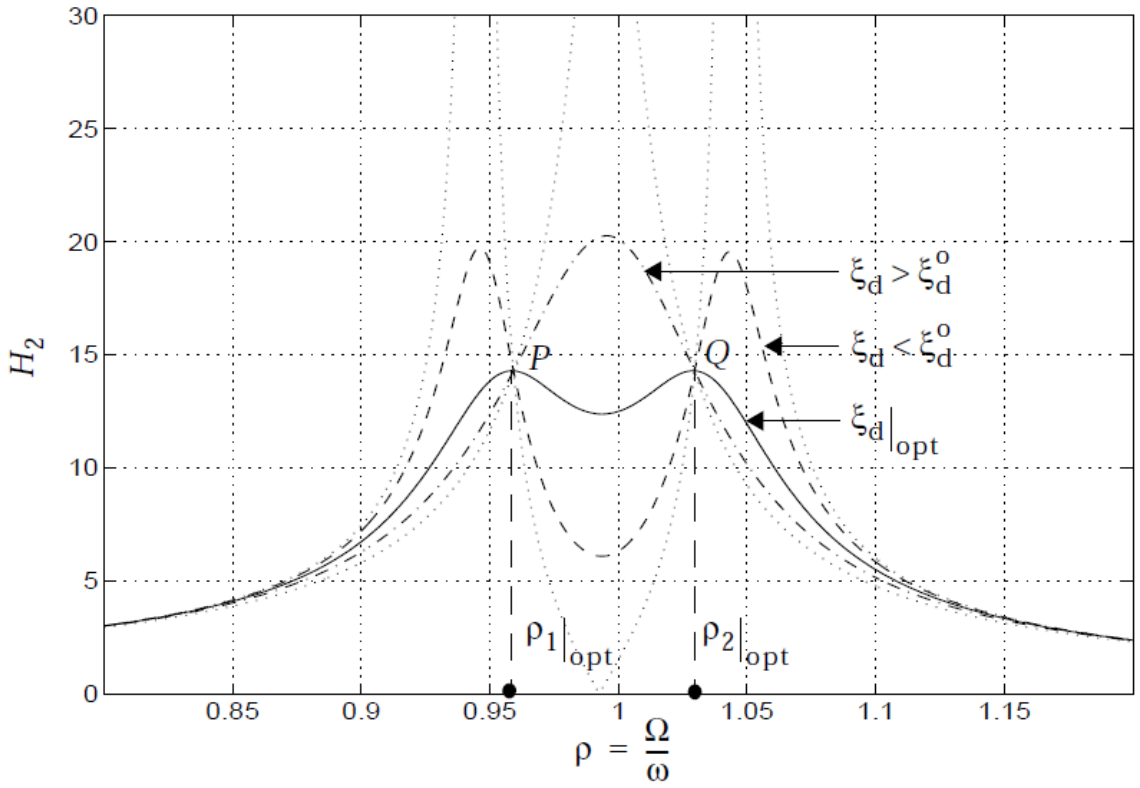

Figure 2.8: H_2 amplification factor vs normalized frequency of the excitation (ω) for an optimal frequency TMD. (Connor, 2003)

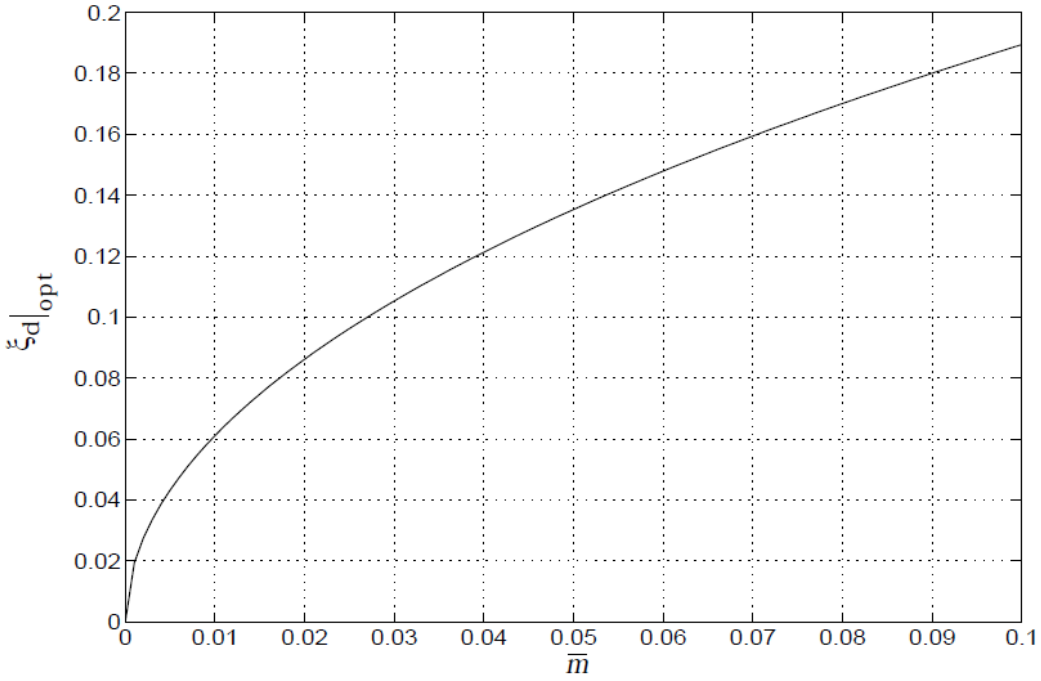

Figure 2.9: Optimal damping ratio versus mass ratio. (Connor, 2003)

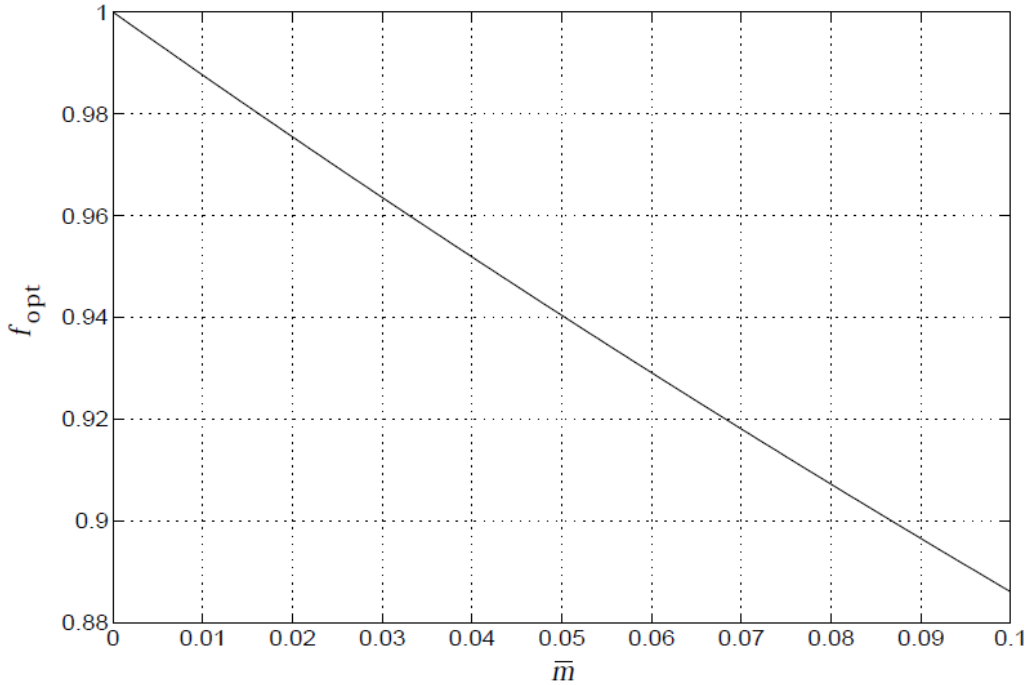

Figure 2.10: Optimal frequency ratio versus mass ratio. (Connor, 2003)

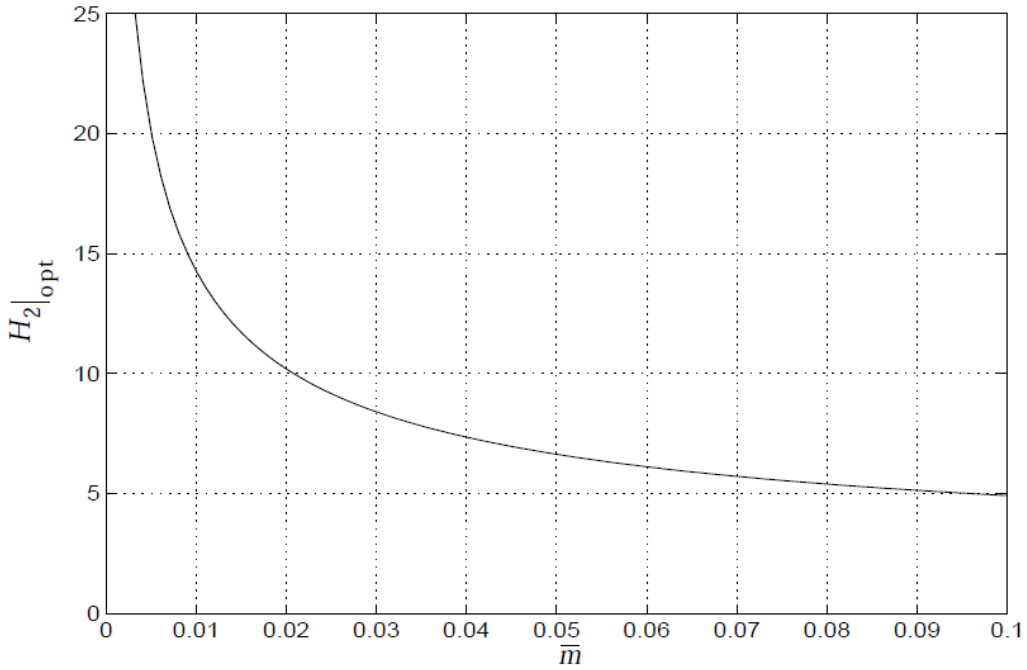

Figure 2.11: H_2 amplification factor for a TMD with optimal damping and frequency versus mass ratio. (Connor, 2003)

Tuned mass dampers have been used in several buildings around the world, including some iconic ones such as Taipei 101 or the Petronas Towers, Figure 2.12 shows the TMD used in the Chilean Chamber of Construction building in Santiago de Chile. The TMD is located at the top floor of the 82.5 [m] building and consists of a steel mass of 150 [Ton] suspended by chains and connected to two viscous dampers.

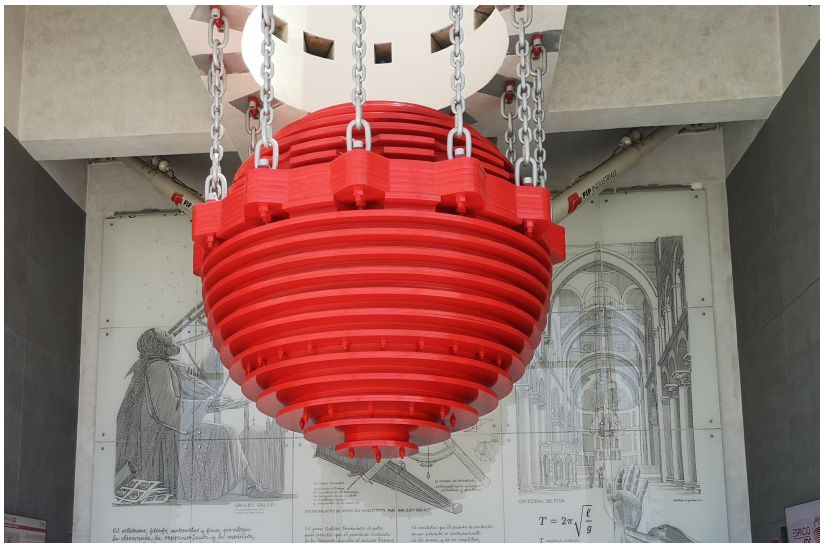

Figure 2.12: TMD installed in the Chilean Chamber of Construction building.

In the case of this study, a TMD will be implemented due to its simplicity of modeling and construction since, in its simplest configuration, it can be modeled as a SDOF system and does not require the fabrication of complex elements. However, the methodology utilized to make real-time hybrid simulation applies to any dynamic system to be tested.

2.2 Methodology

The objective of the experiment is to estimate the response of a three-story structure equipped with a tuned mass damper. For this purpose, the problem is subdivided into a numerical substructure corresponding to a three-story building and an experimental substructure corresponding to the TMD, as presented in Figure 2.13. All displacements are relative to the ground, and the excitation is a ground motion applied as an acceleration on the structure's base.

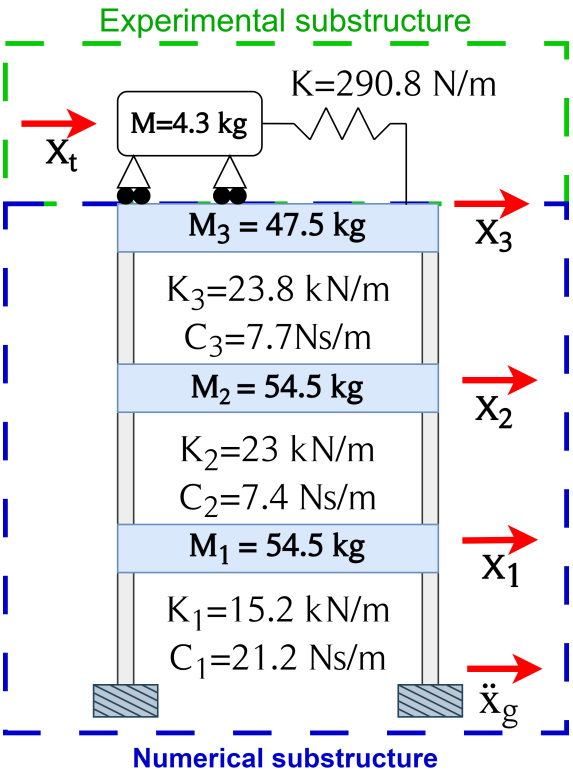

Figure 2.13: Diagram of the structure to be tested.

A shake table in the base of the TMD imposes the absolute displacement of the third floor because the force of the TMD depends on the absolute acceleration of the floor. On the other hand, the force of the TMD over the structure is measured via load cells and used as an input in the numerical simulation, Figure 2.14 shows a simplified diagram of the substructures.

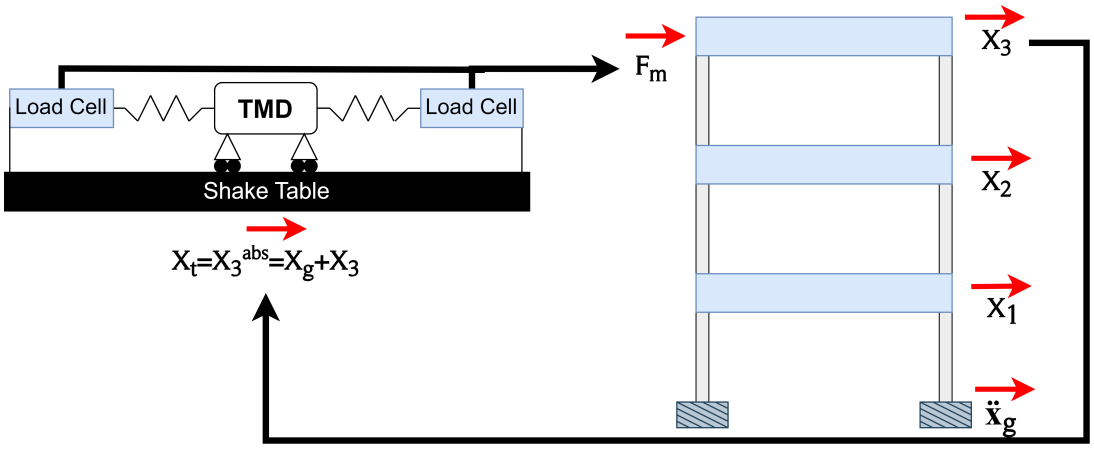

Figure 2.14: Diagram of the substructures.

The equation of motion of the structure equipped with the TMD can be defined as:

$$\begin{bmatrix} \ddot{x}_1 \\ \ddot{x}_2 \\ \ddot{x}_3 \\ \ddot{x}_{TMD} \end{bmatrix} = -[M]^{-1}[K] \begin{bmatrix} x_1 \\ x_2 \\ x_3 \\ x_{TMD} \end{bmatrix} - [M]^{-1}[C] \begin{bmatrix} \dot{x}_1 \\ \dot{x}_2 \\ \dot{x}_3 \\ \dot{x}_{TMD} \end{bmatrix} - [M]^{-1}\{\Gamma\}\ddot{x}_g \tag{2.14}$$

$$\Gamma = \begin{bmatrix} 1 \\ 1 \\ 1 \\ 1 \end{bmatrix} \tag{2.15}$$

$$[M] = \begin{bmatrix} M_1 & 0 & 0 & 0 \\ 0 & M_2 & 0 & 0 \\ 0 & 0 & M_3 & 0 \\ 0 & 0 & 0 & M_{TMD} \end{bmatrix} \tag{2.16}$$

$$[C] = \begin{bmatrix} C_1 + C_2 & -C_2 & 0 & 0 \\ -C_2 & C_2 + C_3 & -C_3 & 0 \\ 0 & -C_3 & C_3 + C_{TMD} & -C_{TMD} \\ 0 & 0 & -C_{TMD} & C_{TMD} \end{bmatrix} \tag{2.17}$$

$$[K] = \begin{bmatrix} K_1 + K_2 & -K_2 & 0 & 0 \\ -K_2 & K_2 + K_3 & -K_3 & 0 \\ 0 & -K_3 & K_3 + K_{TMD} & -K_{TMD} \\ 0 & 0 & -K_{TMD} & K_{TMD} \end{bmatrix} \tag{2.18}$$

Where x_{TMD} is the relative displacement of the TMD to the 3rd floor, K_{TMD} is the stiffness of the TMD, and C_{TMD} is the viscous dissipation of the TMD (this parameter will be assumed close to zero and finally neglected). Note that the TMD force can be calculated as:

$$F_m = M_{TMD}\ (\ddot{x_g} + \ddot{x}_3 + \ddot{x}_{TMD}) \tag{2.19}$$

2.2.1 Numerical substructure

The numerical substructure consists of a three-story shear building with concentrated masses and 1% Rayleigh-type damping fixed to the last two modes. The mass, stiffness, and damping matrices are presented in equations 2.20, 2.21 and 2.22. Using the mass, stiffness, and damping matrices,

the state-space model of the system presented in equations 2.27 and 2.28 is constructed where: x is a vector containing the positions and velocities of each story; u a vector containing the basal acceleration and the restoring force of the TMD; y is the response vector of the structural system. Note that the output of the response vector is the absolute displacement of the third floor (target displacement) that will be compensated later.

$$[M] = \begin{bmatrix} 54.5 & 0 & 0 \\ 0 & 54.5 & 0 \\ 0 & 0 & 47.5 \end{bmatrix} [\text{kg}] \tag{2.20}$$

$$[C] = \begin{bmatrix} 28.6 & -7.4 & 0 \\ -7.4 & 31.3 & -7.7 \\ 0 & -7.7 & 21.8 \end{bmatrix} \left[\frac{\text{Ns}}{\text{m}}\right] \tag{2.21}$$

$$[K] = \begin{bmatrix} 38.2 & -23.0 & 0 \\ -23.0 & 46.8 & -23.8 \\ 0 & -23.8 & 23.8 \end{bmatrix} \left[\frac{\text{kN}}{\text{m}}\right] \tag{2.22}$$

$$\Gamma = \begin{bmatrix} 1 \\ 1 \\ 1 \end{bmatrix} \tag{2.23}$$

$$\begin{bmatrix} \ddot{x}_1 \\ \ddot{x}_2 \\ \ddot{x}_3 \end{bmatrix} = -[M]^{-1}[K] \begin{bmatrix} x_1 \\ x_2 \\ x_3 \end{bmatrix} - [M]^{-1}[C] \begin{bmatrix} \dot{x}_1 \\ \dot{x}_2 \\ \dot{x}_3 \end{bmatrix} - [M]^{-1}\{\Gamma\}\ddot{x}_g - [M]^{-1} \begin{bmatrix} 0 \\ 0 \\ 1 \end{bmatrix} F_m \tag{2.24}$$

$$\begin{aligned} \{\dot{x}\} &= [A_s]\{x\} + [B_s]\{u\} \\ \{y\} &= [C_s]\{x\} + [D_s]\{u\} \end{aligned} \tag{2.25}$$

$$\{x\} = \begin{bmatrix} x_1 & x_2 & x_3 & \dot{x}_1 & \dot{x}_2 & \dot{x}_3 & x_g & \dot{x}_g \end{bmatrix}^T, \quad \{u\} = \begin{bmatrix} \ddot{x}_g & F_m \end{bmatrix}^T \tag{2.26}$$

$$[A_s] = \begin{bmatrix} [0]_{3x3} & [I]_{3x3} & [0]_{3x2} \\ -[M]^{-1}[K] & -[M]^{-1}[C] & [0]_{3x2} \\ [0]_{2x3} & [0]_{2x3} & \begin{bmatrix} 0 & 1 \\ 0 & 0 \end{bmatrix} \end{bmatrix} \tag{2.27}$$

$$[B_s] = \begin{bmatrix} [0]_{3x1} & [0]_{3x1} \\ -[M]^{-1}\{\Gamma\} & -[M]^{-1}\begin{bmatrix} 0 \\ 0 \\ 1 \end{bmatrix} \\ [0]_{2x1} & \begin{bmatrix} 0 \\ 1 \end{bmatrix} \end{bmatrix} \tag{2.28}$$

$$[C_s] = \begin{bmatrix} 0 & 0 & 1 & 0 & 0 & 0 & 1 & 0 \end{bmatrix}, \quad [D_s] = \begin{bmatrix} 0 & 0 \end{bmatrix} \tag{2.29}$$

2.2.2 Experimental Substructure

The experimental substructure consists of an aluminum reaction frame on which two SBR16 rails are mounted, and over the rails, an inertial mass slides on linear bearings. The platform is connected to the frame by two extension springs using a bolted connection with a total stiffness of 290.8 [N/m]. The TMD is tuned to the first fundamental frequency of the numerical substructure using a set of variable masses with a total mass of 4.28 [kg]; load cells are installed in line with the springs to measure the restoring force directly. A digital model of the TMD and a schematic diagram are shown in Figure 2.15 and Figure 2.16 shows the experimental setup used in the laboratory.

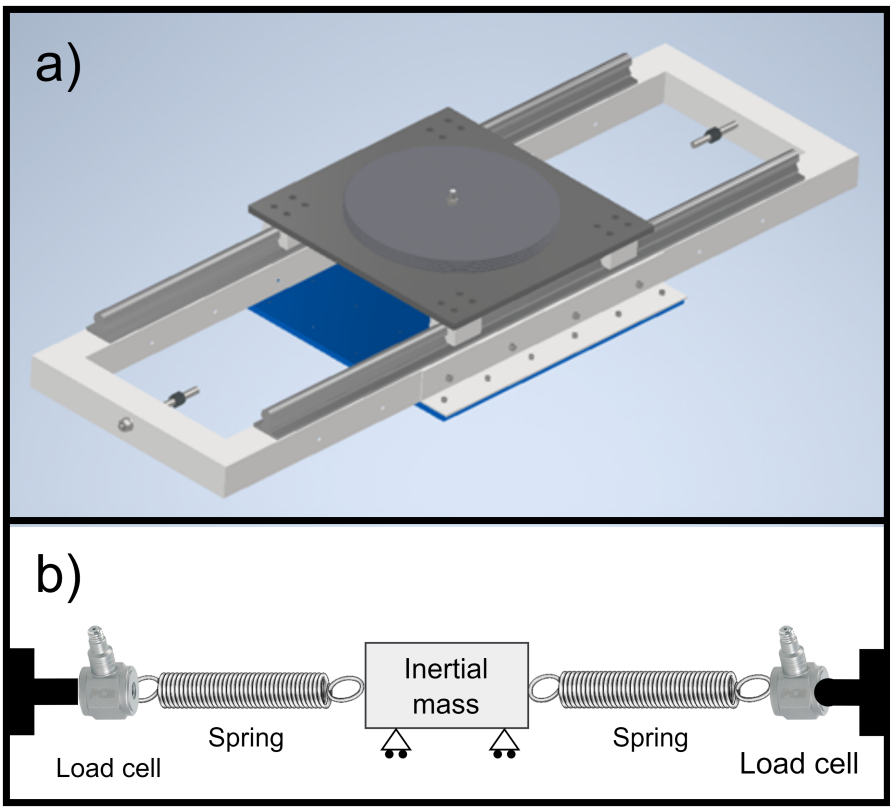

Figure 2.15: a) Digital model of the experimental substructure; b) Experimental TMD simplified diagram.

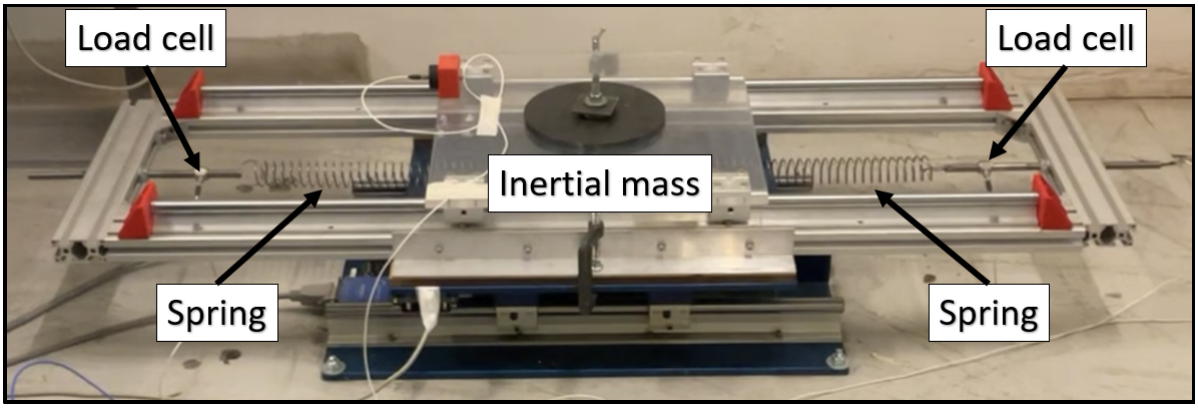

Figure 2.16: Experimental substructure.

2.2.3 Hardware

A dSpace Microlabox III real-time controller (dSpace, 2020) is used to perform the test, in which the displacements of the numerical substructure are solved and then imposed on the experimental substructure using a "Shake Table II" electromechanical shake table (Quanser, 2017). The shake table is driven by a DC motor controlled by displacement using a rotary encoder and a PD controller. The TMD restoring force measurement is performed using two PCB 208C05 load cells (PCB Electronics, 2016) in line with the springs. The position of the table is obtained from a rotary encoder and the pitch of the ball screw that moves the shake table. A simplified diagram of the experiment is presented in Figure 2.17.

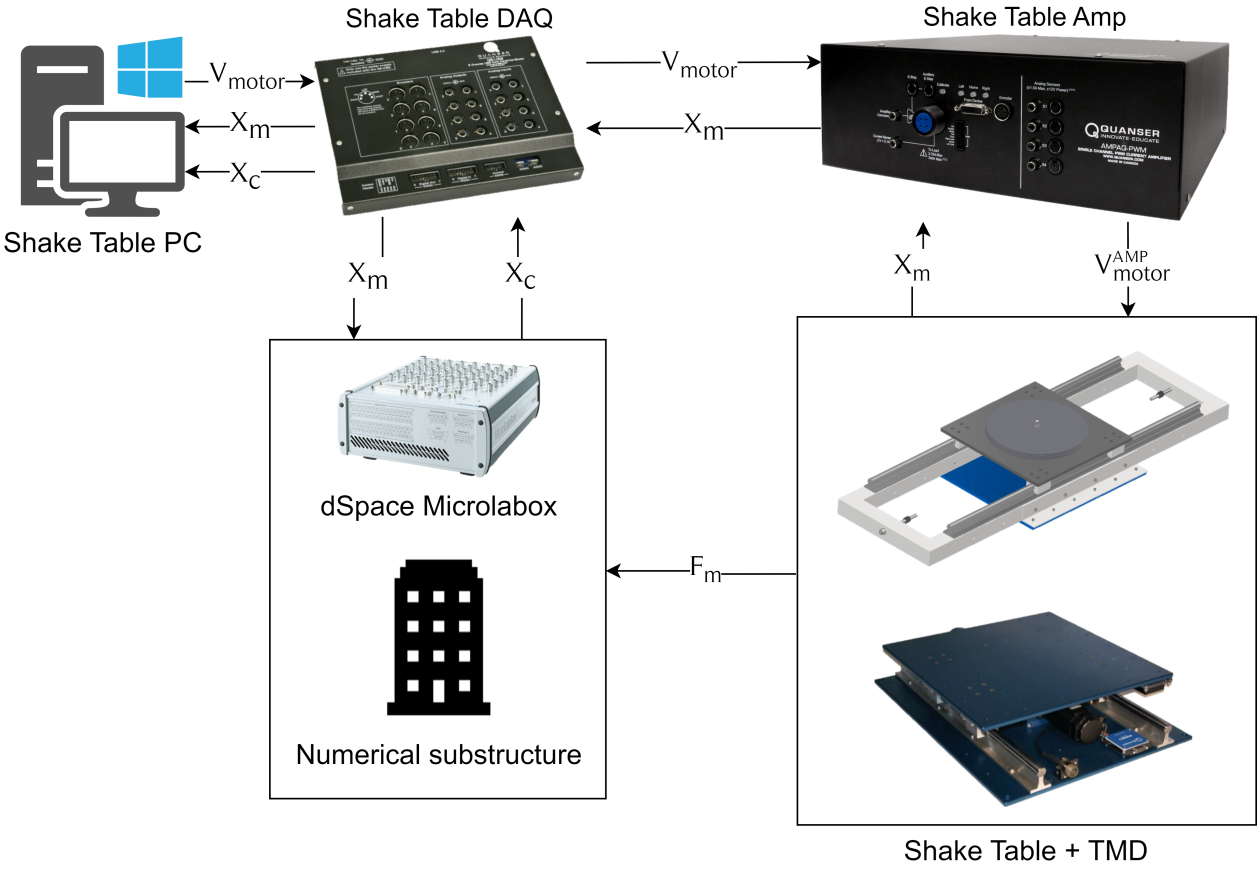

Figure 2.17: Simplified diagram of the hardware used in the tests.

2.2.4 Identification of the control plant

To identify the control plant, a test is performed using as excitation of the shake table a band-limited white noise with the parameters indicated in Table 2.1 and a mass equivalent to the mass of the experimental substructure.

Table 2.1: Parameters of band-limited white noise

Parameter	Value
RMS displacement [mm]	1.5
Bandwidth [Hz]	0 - 20

From the target versus measured position data, spectral power density functions are calculated to construct the H_1 and H_2 estimators presented in Equation 2.30 and obtain an estimation of the frequency response function of the system.

$$\begin{aligned} H_1(f) &= \frac{X(f)F^*(f)}{F(f)F^*(f)} = \frac{G_{XF}}{G_{FF}} \\ H_2(f) &= \frac{X(f)X^*(f)}{F(f)X^*(f)} = \frac{G_{XX}}{G_{FX}} \end{aligned} \tag{2.30}$$

Where G_{XX} and G_{FF} correspond to the spectral power density with themselves of the input and output, G_{FX} and G_{XF} correspond to the cross-spectral power density.

Finally, an estimation of the frequency response function with three poles in the denominator and no zeros in the numerator is performed using the methodology proposed by Kim et al. (2005). The results are presented in Figure 2.18, and the identified system equation is shown in Equation 2.31; note that the identified system is restricted to $F(0) = 1$ to fix the "static" condition. Since the excitation frequency is limited from 0 to 20 [Hz] the results are shown in the same range; however, the identified model is a continuous transfer function that extrapolate the system's frequency response function over this frequency range.

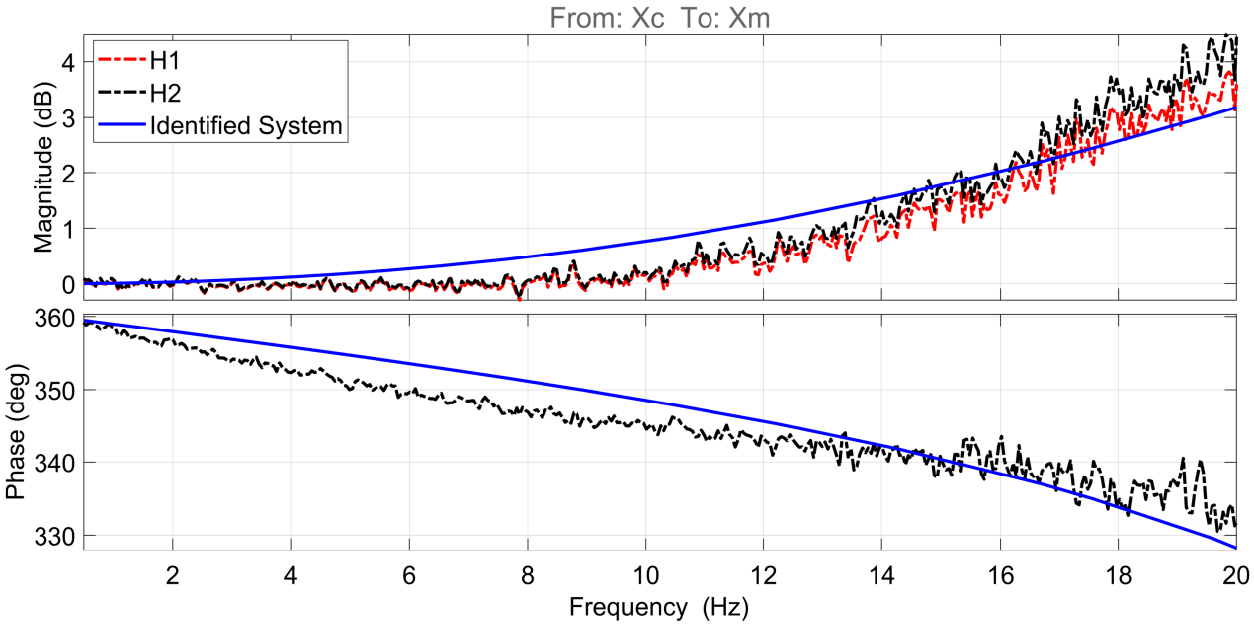

Figure 2.18: H_1 and H_2 estimation of the transfer function

$$F(\omega) = \frac{38420}{-w^2 + 110.8\omega i + 38420} \tag{2.31}$$

2.2.5 Feedforward compensator

The frequency response function is taken to the Laplace domain, and the feedforward compensator is constructed by inverting the transfer function of the control plant. For the numerical implementation of the compensator, the realization in time presented in Equation 2.32 is used, where the first and second-order derivatives are approximated using third-order finite differences whose formulation is shown in Equation 2.33.

$$\begin{gathered} \mathrm{F(s)} = \frac{\mathrm{s}^2 + 110.8\ \mathrm{s} + 38420}{38420} X(s) \\ \mathcal{L}^{-1}\left\{as^2X(s) + bsX(s) + c\right\} = a\ddot{x}(t) + b\dot{x}(t) + cx(t) \\ x_c(t) = \frac{1}{38240}\ddot{x}_t(t) + \frac{110.8}{38420}\dot{x}_t(t) + x_t(t) \end{gathered} \tag{2.32}$$

Where x_c corresponds to the commanded position and x_t to the target position.

$$\begin{gathered} x(t = T) = x^k \\ x(t = T - \Delta t) = x^{k-1} \\ \dot{x}^k \approx -\frac{1}{3}x^{k-3} + \frac{3}{2}x^{k-2} - 3x^{k-1} + \frac{11}{16}x^k \end{gathered} \tag{2.33}$$

Finally, Figure 2.19 shows the frequency response function of the feedforward compensator where it can be observed that frequencies below 40 [Hz] are reduced to mitigate the dynamic amplification produced by the actuator-structure interaction.

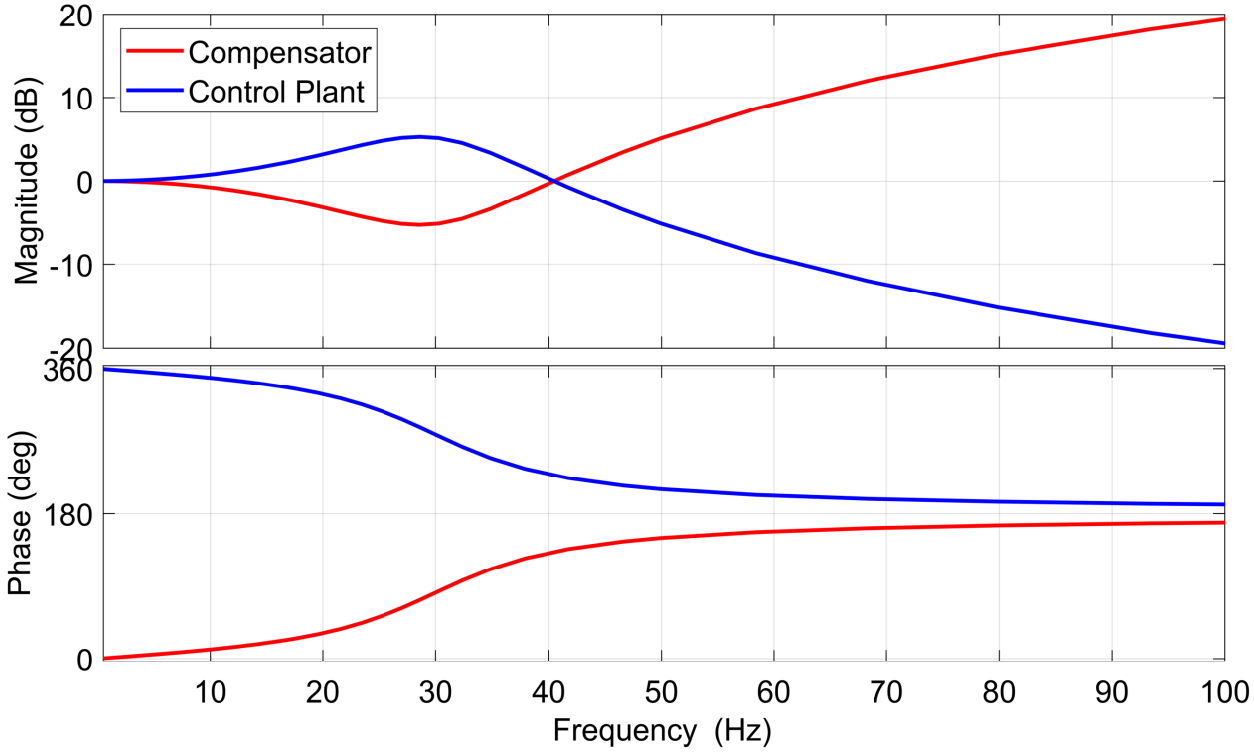

Figure 2.19: Feedforward compensator to mitigate the effects of actuator-structure dynamics.

It is worth noticing that the compensator amplifies the signals for high frequencies, so special care must be taken with the high-frequency noise produced by electrical interferences so as not to cause instabilities produced by the compensation. However, part of the electrical noise of the measured force should be canceled because the net force is obtained by subtracting both load cell measures. Also, the numerical substructure response decays quickly with the frequency, acting as a lowpass filter. Based on this information, no extra poles will be added to the compensator.

2.2.6 Test protocol

To avoid drift issues, the tests were performed using four scaled and baseline-corrected seismic records. The ground motions and test duration are detailed in Table 2.2. Moreover, the experiments duration are established considering the duration of the seismic record and the free vibration response to evaluate the stability of the hybrid system.

Table 2.2: Ground motions used for the experiment.

Ground Motion	Station	Scale Factor	Test duration [s]
El Centro 1979 (Imperial Valley)	El Centro	10%	70
Northridge 1994	Sylmar Olive View Med FF	12%	70
Kobe 1995	HIK	40%	170
Maule 2010	Concepción	12%	200

The numerical substructure is integrated using the Runge-Kutta 4^{th} Order algorithm in MATLAB/Simulink using a fixed time step of 0.001 [s], just like the shake table control algorithm. A block diagram of the algorithm is shown in Figure 2.20.

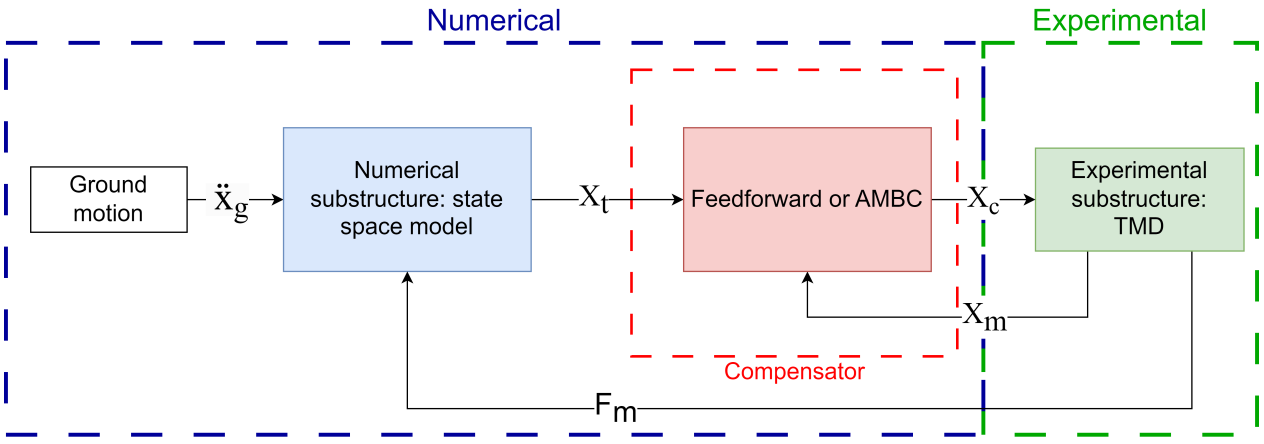

Figure 2.20: Block diagram of the experiment.

2.2.7 Error indicators

Since usually the effects of actuator-structure dynamics cannot be completely mitigated, some authors have proposed using performance indicators for RTHS. In particular, in this study, some of the indicators proposed by Silva et al. (2020) will be used, which are defined in equations 2.34, 2.35 and 2.36 for any two signals X and Y. These indicators measure the average delay, tracking error and peak error, respectively.

$$J_1 = \arg\max_k \left(\sum_i \mathbf{y}_{\mathrm{n}}^{(1)}(i) x_{\mathrm{m}}(i-k) \right) \tag{2.34}$$

$$J_2 = \sqrt{\frac{\sum_{i=1}^{N} \left[x_{\mathrm{m}}(i) - \mathbf{y}_{\mathrm{n}}^{(1)}(i) \right]^2}{\sum_{i=1}^{N} \left[\mathbf{y}_{\mathrm{n}}^{(1)}(i) \right]^2}} \times 100\% \tag{2.35}$$

$$J_3 = \frac{\max \left| x_{\mathrm{m}}(i) - \mathbf{y}_{\mathrm{n}}^{(1)}(i) \right|}{\max \left| \mathbf{y}_{\mathrm{n}}^{(1)}(i) \right|} \times 100\% \tag{2.36}$$

Average delay is important because Horiuchi et al. (1999) proved that delay acts as a negative damping and can lead the system to instability. On the other side, J_2 and J_3 represent the magnitude of the error in terms of amplitude, which is essential to ensure test accuracy. In particular, RMS error is a good indicator of the overall performance of the compensator. However, large but infrequent errors tend to dilute inside the mean, but they still can negatively affect results, so peak error is a better indicator for these cases.

2.3 Results and analysis

2.3.1 Sinchronization

To evaluate the correspondence between the target and measured signals, both signals are plotted against each other as shown in Figure 2.21. Also, a least square linear fit is performed to measure the linear correlation between the signals. It can be observed that the slope of the adjustments ranges between 0.9995 and 1.0009, with a bias between 0.0011 and 0.0022 [cm]. Additionally, the values of R^2 show an excellent linear correlation between measured and target signals.

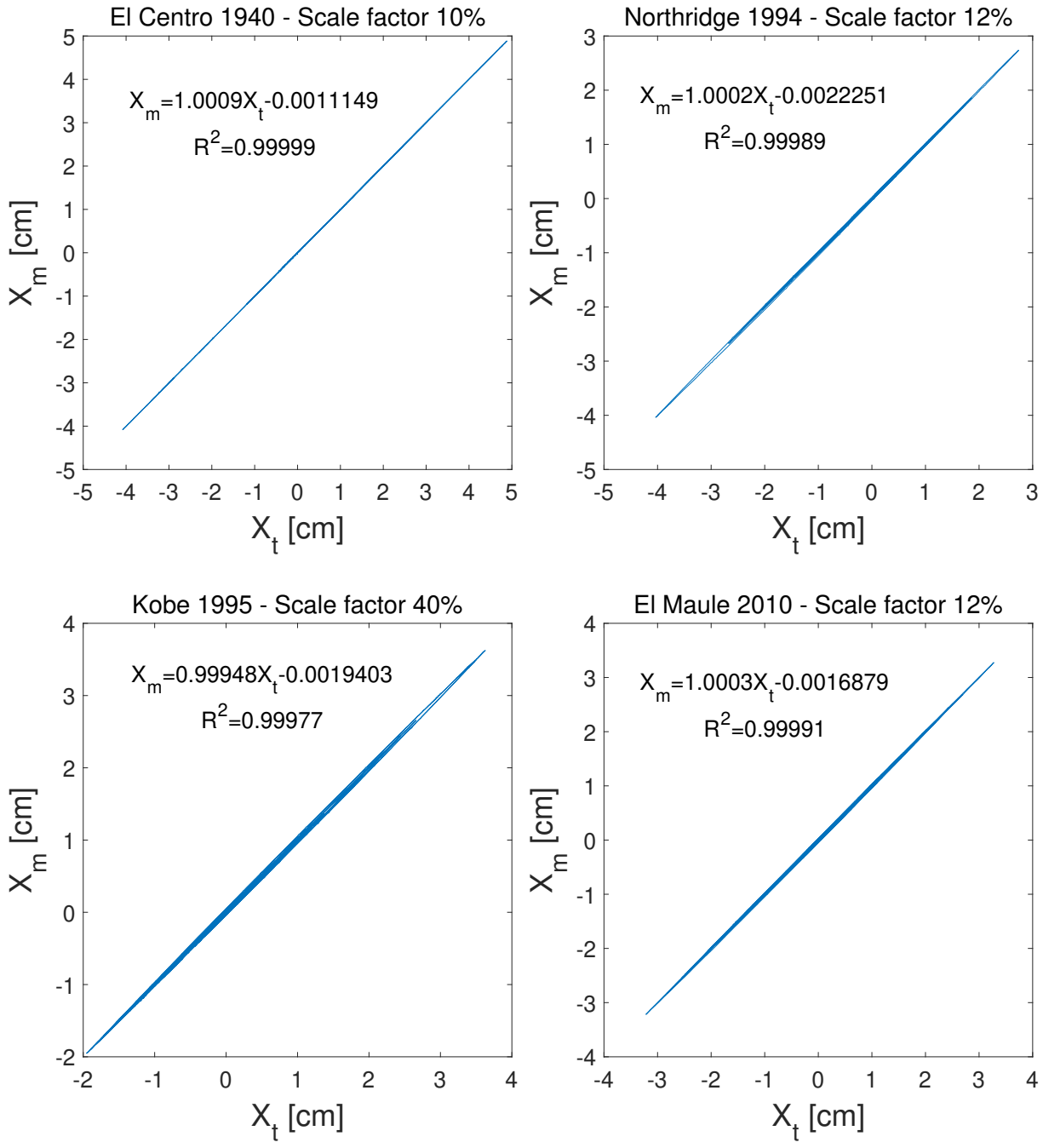

Figure 2.21: Subspace synchronization plots of the four ground motions tested.

The subspace synchronization plots (SSP) show excellent performance in terms of delay, usually seen as an oval form of the plots, with a slight detriment in Kobe's case. The results obtained for the bias are of the order of hundredths of a millimeter, which can be considered negligible for the purposes of this test.

2.3.2 Time history

The results presented in Figure 2.22 show the position of the shake table versus time, corresponding to the absolute displacement of the third floor of the numerical substructure. The system is stable for the four ground motions tested with a residual displacement near zero, which agrees with expectations.

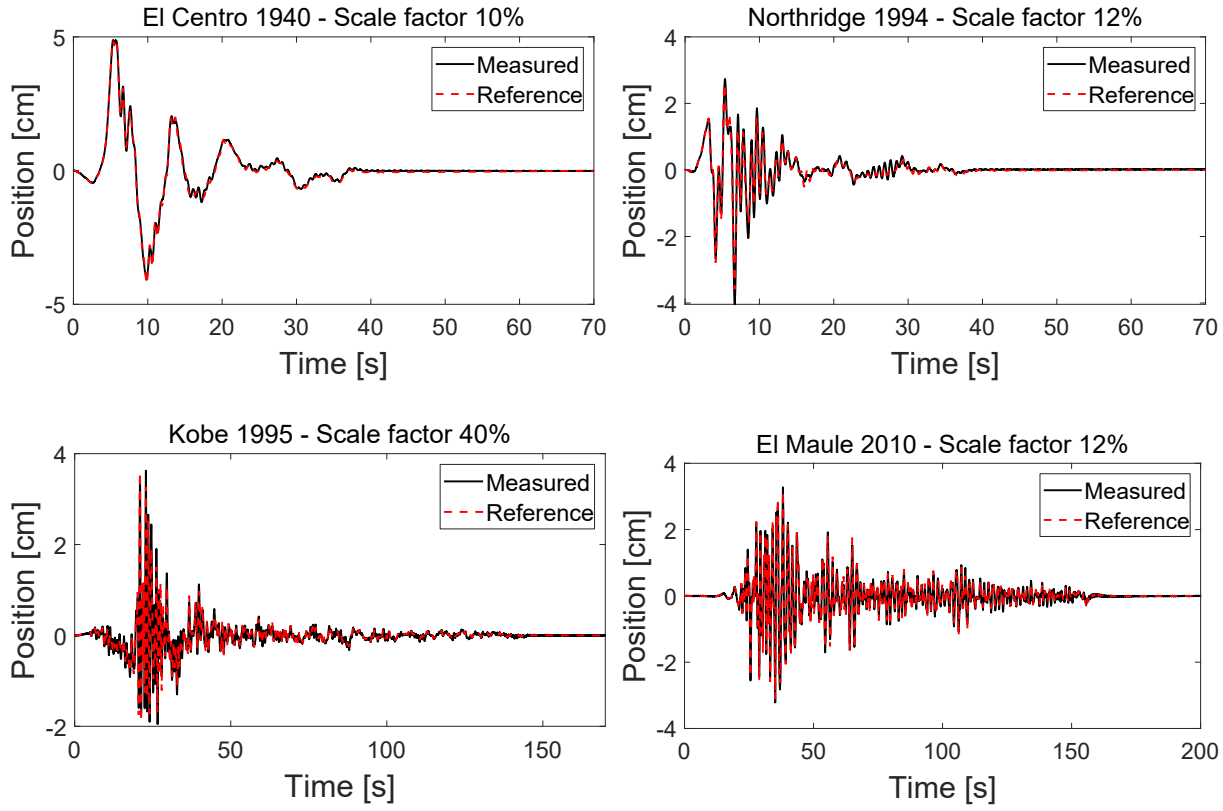

Figure 2.22: Time history plots full length.

On Figure 2.23, a zoomed-in version of the Figure 2.22 is presented to visualize the correspondence between the results of the RTHS and a numerical model. The reference model of the experimental substructure is constructed from identified properties of the TMD subjected to a band-limited white noise (BLWN) in a separate test. The results correlate well with the reference model's response with a higher error in the case of the Kobe seismic record. Note that the maximum displacement is similar between the experimental and numeric responses for all cases.

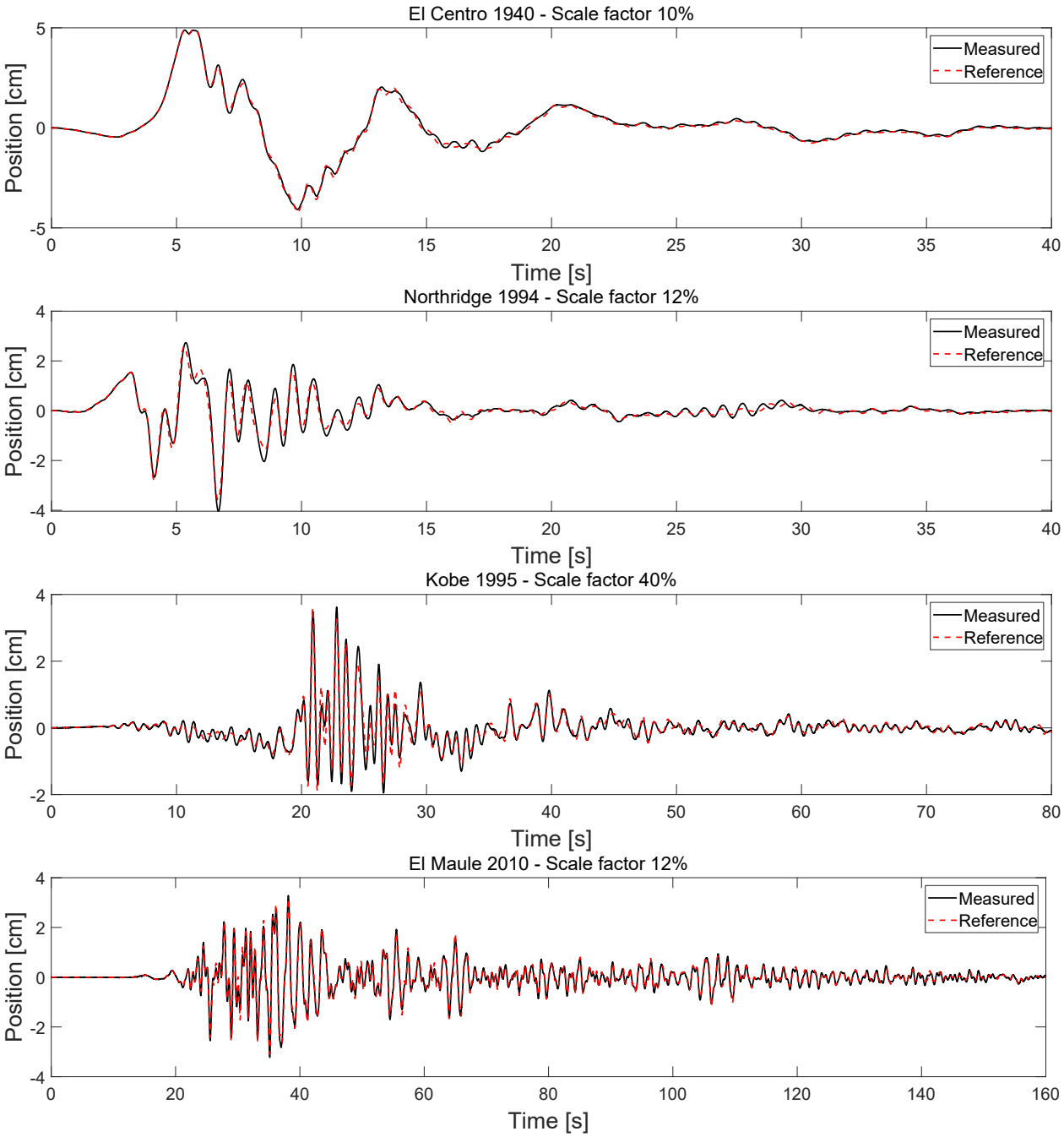

Figure 2.23: Time history plots zoomed in for better visualization.

Based on the results, the experiment performed well with values corresponding to the reference model. However, there are differences between the measured and reference responses, which is to be expected because the reference model used is a simplified model with one degree of freedom that does not capture all the phenomena that occur in reality, such as the small nonlinearity due to the friction between the rail and the bearings. Also, measurements are not perfect and they are

subjected to instrumental error and electrical noise which also lead to differences between measured and reference.

2.3.3 Error index

The results presented in Figure 2.24 show that the average delay of the tests is 2 [ms] and remains constant independent of the seismic record. On the other hand, both the root mean square error and the maximum absolute error remain bounded below 2%, indicating a good compensator performance.

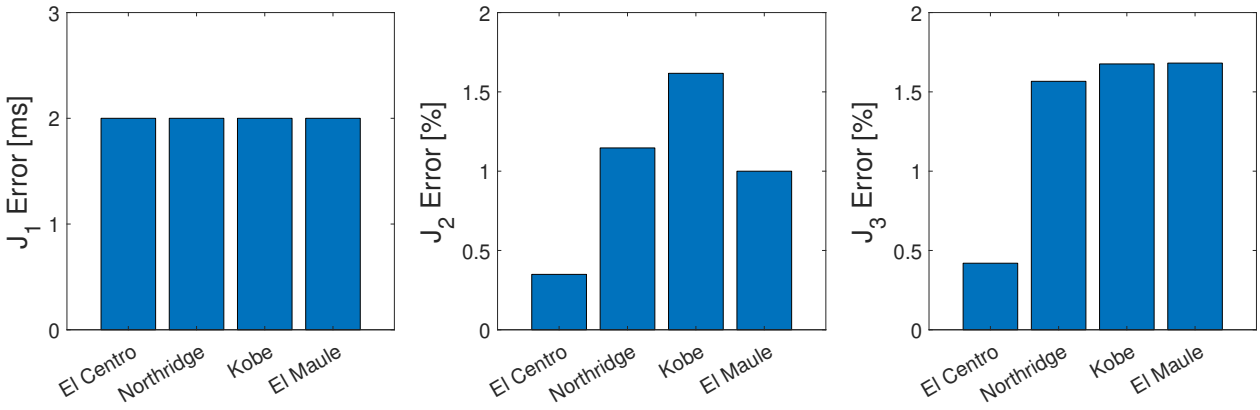

Figure 2.24: J_1, J_2, J_3 Error.

It is worth noticing that even when the results show that for all ground motions, the average delay is 2 [ms], there may be differences of less than 1 [ms] that are not observable due to the timestep of the experiment and the method used to calculate the delay. On the other hand, the best results in terms of J_2 and J_3 are obtained for El Centro, which is attributed to its low-frequency content compared to the other three ground motions.

2.4 Summary

This chapter presents a real-time hybrid simulation test of a three-story structure equipped with a tuned mass damper using an electromechanical shake table and dynamic compensation. From the results obtained, it is observed that the J_1 error presents an average delay of 2 [ms], which is within the expected order of magnitude for RTHS and does not introduce numerical instabilities to the system. The J_2 and J_3 errors are below 2%, which, together with the results of the least squares fit of the SSP, shows a good performance of the feedforward compensator. In addition, the four cases analyzed are stable, with residual deformations tending to zero in the free oscillations

phase. On the other hand, the slight differences between the reference and experimental results are attributable to the fact of that the result of the reference model corresponds to a simplification of the problem where behaviors such as friction or nonlinearity in the springs are not considered. Nevertheless, the measured results are similar to those obtained from a reference model in terms of maximum amplitudes and time response, therefore, the results validate the methodology and hardware implemented and can be used for further RTHS studies.

Chapter 3

Experimental validation of the performance of the robust adaptive model-based compensator for real-time hybrid simulation

3.1 Literature review

3.1.1 Adaptive compensation

Adaptive compensation is one of the alternatives to fixed parameter compensators, like the feedforward compensator. The main idea is to adjust the parameters of the compensator to reduce error on the fly so the compensator can adapt to changes in the control plant, like nonlinear behavior or time-variant parameters. Typically, adaptive control strategies can be divided into control law and adaptive law. The first defines the control strategy to control the system, and the second one is used to adjust the parameters of the control law. Methods like the tracking error-based adaptive compensation use a simple transfer function model and adjust the parameter based on the synchronization error (C. Chen & Ricles, 2010). Other methods used adaptive laws based on frequency response data, just like the adaptive phase lead compensator, where the adaptive parameters are calculated using a "moving FFT" (Tao & Mercan, 2019).

Another way to build a compensator is by using a feedforward control law with a polynomial estimation of the transfer function with adaptive parameters. One example of this approach is the adaptive time series (ATS), where the structure-actuator interaction is modeled with a polynomial expression and adjusted with the least square method (Chae et al. 2013). In similar approach, Palacio-Betancur and Soto (2019) proposed the conditional adaptive time series (CATS) that uses the same control law as the ATS, but the adaptive law uses the recursive least square method instead of the least square method. The recursive least square method is less computationally intensive than the least square method (Palacio-Betancur & Soto, 2019), but requires setting parameters based on the designer's experience which can be challenging. Also, CATS is capable of mitigating instabilites due to small signal-to-noise ratios (SNR), for example, during free vibrations in a RTHS test.

Other methods of compensation use estimations of actuator-structure interaction based on models with physical properties; for example, the AMBC is designed based on a model of the structure-actuator interaction to set a feedforward compensator and an adaptive law based on error gradient (P. C. Chen et al. 2015). Some researchers have presented similar implementations but with different adaptive laws based on the Kalman filter, like the MPC (Tsokanas et al. 2022) or the MAC-KF (Xu et al. 2023). There is also a mixed data-driven approach where part of the compensator is built based on a model and later calibrated based on data using reinforcement learning techniques (Li et al. 2022).

Compensators based on models are of particular interest to this study because the objective is

to validate the robust approach of adaptive model-based compensator presented by Gálmez and Fermandois (2020), which is derived from the adaptive model-based algorithm proposed by P. C. Chen et al. (2015).

3.1.1.1 Adaptive model based compensator

The adaptive model-based compensator (Fermandois et al. 2020) can be divided into two main parts and is illustrated in Figure 3.1. First, the feedforward compensator that corresponds to an inverse of the nominal model of the structure-actuator interaction, the inputs of the feedforward are the target signal (x_t), it is derivatives (depending on the order of the model), and the adaptive parameters [A]. Second, the adaptive law takes the commanded and measured signals to estimate the new adaptive parameters in a closed-loop scheme. To avoid undesired noise amplification, the signals are filtered before entering the adaptive law algorithm; these filters are designed with a cut-off frequency depending on the expected frequency content of the signals.

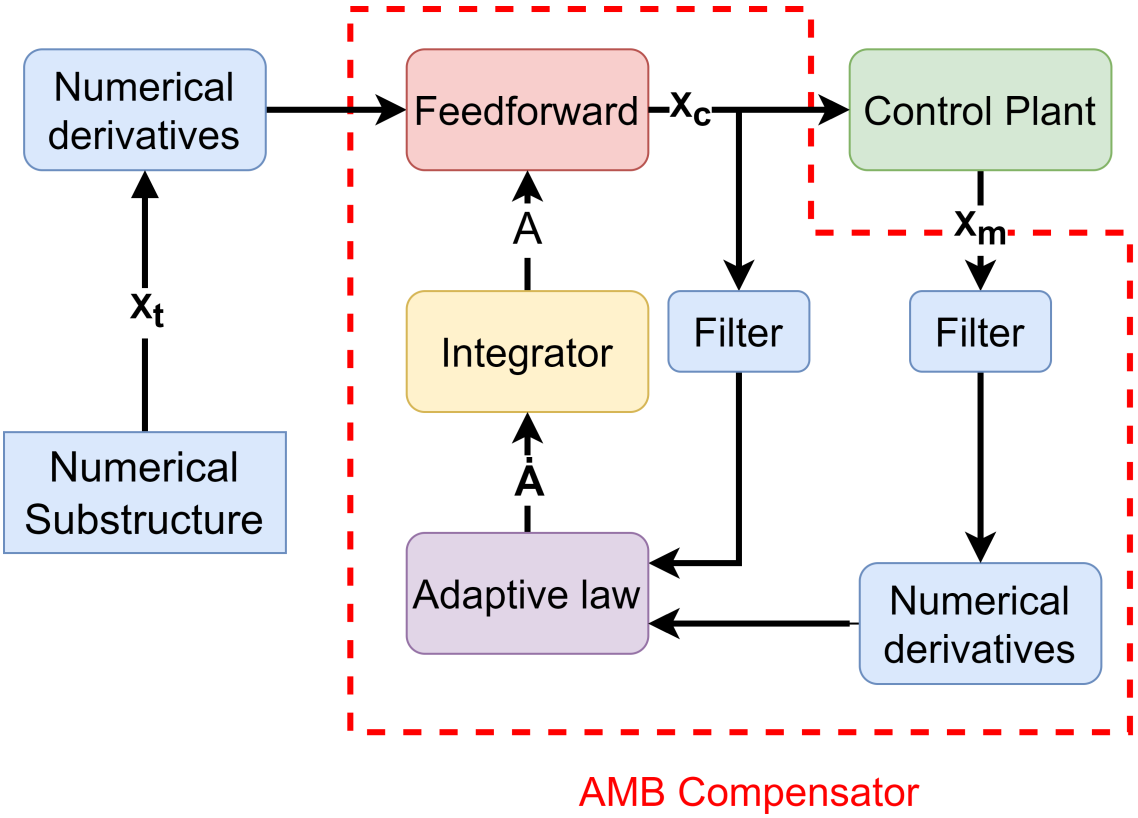

Figure 3.1: Block diagram of the AMB compensator algorithm.

The adaptive law of the AMBC is governed by the Equation 3.1

$$\dot{A} = \Gamma e X_m \tag{3.1}$$

Where e is an error parameter (Equation 3.2), $\hat{x}_c$ is an estimation of the commanded signal (Equation 3.3), m_s^2 is a normalization parameter (Equation 3.4), Γ is a set of adaptive gains defined by the designer, x_c is the commanded signal, x_m is the measured signal and, X_m is vector of the measured signal and its derivatives.

$$e = \frac{x_c - \hat{x}_c}{m_s^2} \tag{3.2}$$

$$\hat{x}_c = \begin{bmatrix} a_0 & a_1 & a_2 & a_3 \end{bmatrix} \begin{bmatrix} x_m & \dot{x}_m & \ddot{x}_m & \dddot{x}_m \end{bmatrix}^T \tag{3.3}$$

$$m_s^2 = 1 + \left(X_m^T X_m\right) \tag{3.4}$$

Gálmez and Fermandois (2020) proposed that to obtain a robust controller, Γ gains would be estimated considering the uncertainty of the model parameters of the actuator-structure interaction model. This estimation is done by minimizing Equation 3.5 that is the average RMS tracking error (Equation 3.6) of a set of N realizations of the system, where every simulation has random parameters based on the uncertainty of the control plant, numerical substructure and ground motions.

$$P\left(\Gamma_k\right) = \frac{1}{N} \sum_{n=1}^{N} J_{2n}\left(\Gamma_k\right) \tag{3.5}$$

$$J_{2n}\left(\Gamma_k\right) = \frac{\mathbb{E}\left[\left(x_{tn} - x_{mn}\right)^2\right]}{\mathbb{E}\left[x_{tn}^2\right]} \tag{3.6}$$

The calibration process proposed by Gálmez and Fermandois (2020) is described in Figure 3.2.

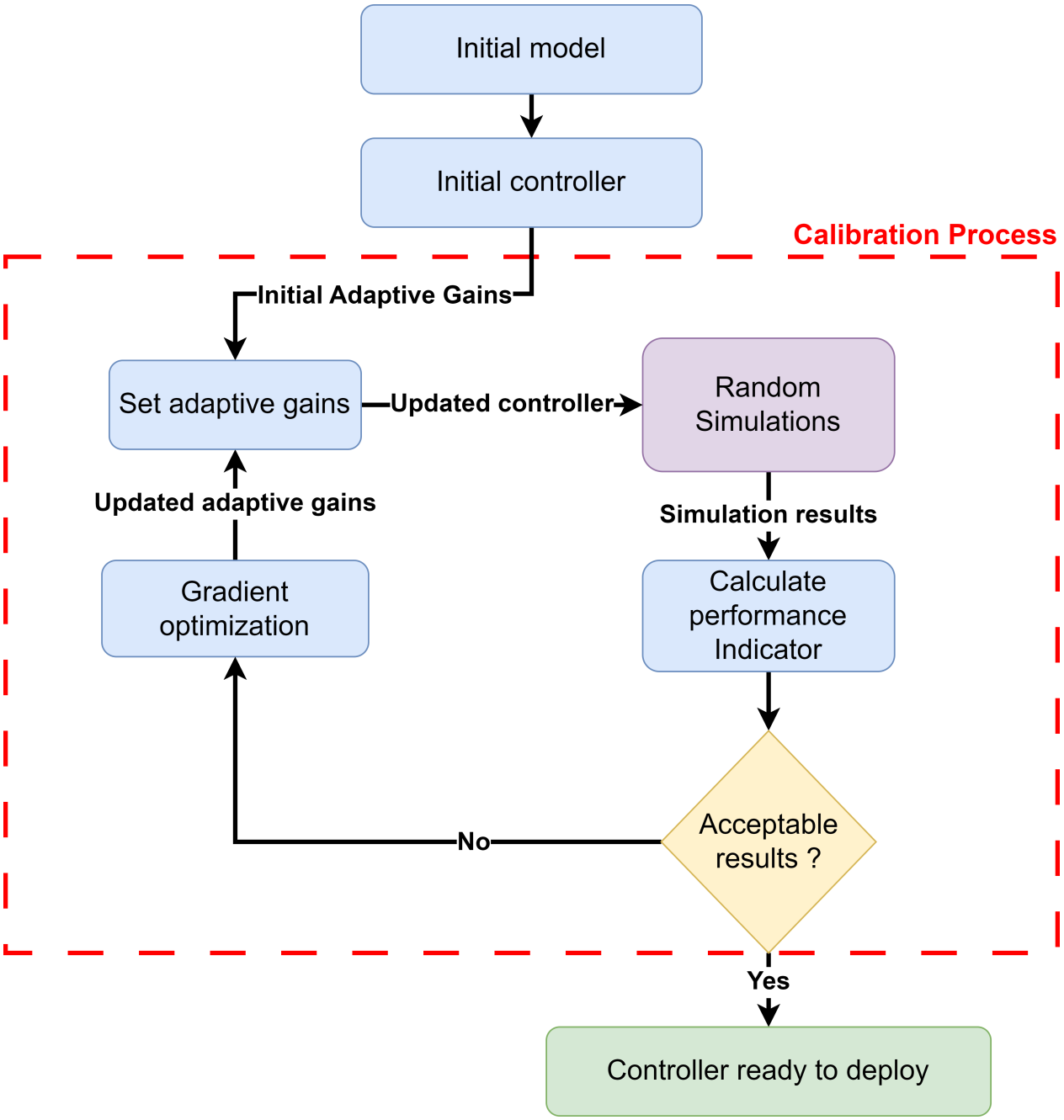

Figure 3.2: Calibration process of the AMB compensator algorithm (adapted from Gálmez and Fermandois, 2020).

3.2 Methodology

The structure to be tested in this experiment is a three-story shear building with masses concentrated on each floor and 1% Raygleigh type damping fixed to the last two modes, similar to the one presented in Chapter 2. However, the inter-story stiffness has been modified to increase the structure's natural frequency and maximize the third floor's PFA with a stroke limitation of ±5 [cm].

The system is simulated using MATLAB and a state-space model of the structure equipped with the TMD. The mass matrix is equal to the one presented in Chapter 2, and to increase the structure's natural frequency, the system's stiffness is multiplied by a scalar parameter β (this parameter is not related to Rayleigh damping parameters). Besides, to maintain the damping ratio close to 1%, the C matrix is calculated as Rayleigh-type damping fixed to the second and third modes of the structure. On the other hand, the stiffness of the TMD is fixed to 756 $\frac{kN}{m}$ which corresponds with the stiffer spring available in the laboratory. To tune the TMD, the mass is modified to match the first natural frequency of the structure. The equation of motion of the system is shown in Equation 3.7

$$\begin{bmatrix} \ddot{x}_1 \\ \ddot{x}_2 \\ \ddot{x}_3 \\ \ddot{x}_{TMD} \end{bmatrix} = -[M]^{-1}\beta[K] \begin{bmatrix} x_1 \\ x_2 \\ x_3 \\ x_{TMD} \end{bmatrix} - [M]^{-1}[C] \begin{bmatrix} \dot{x}_1 \\ \dot{x}_2 \\ \dot{x}_3 \\ \dot{x}_{TMD} \end{bmatrix} - [M]^{-1}\{\Gamma\}\ddot{x}_g \tag{3.7}$$

$$\Gamma = \begin{bmatrix} 1 \\ 1 \\ 1 \\ 1 \end{bmatrix} \tag{3.8}$$

The response is simulated for $\beta = [1, 10]$ in 0.09 increments, and the resulting PFA of the third floor is plotted against the first natural frequency of the structure. Figure 3.3 shows the maximum 3rd-floor acceleration as a function of the first natural frequency of the structure. Note that because every ground motion has a different frequency content, the natural frequency that maximizes the PFA of the third floor is different for every ground motion.

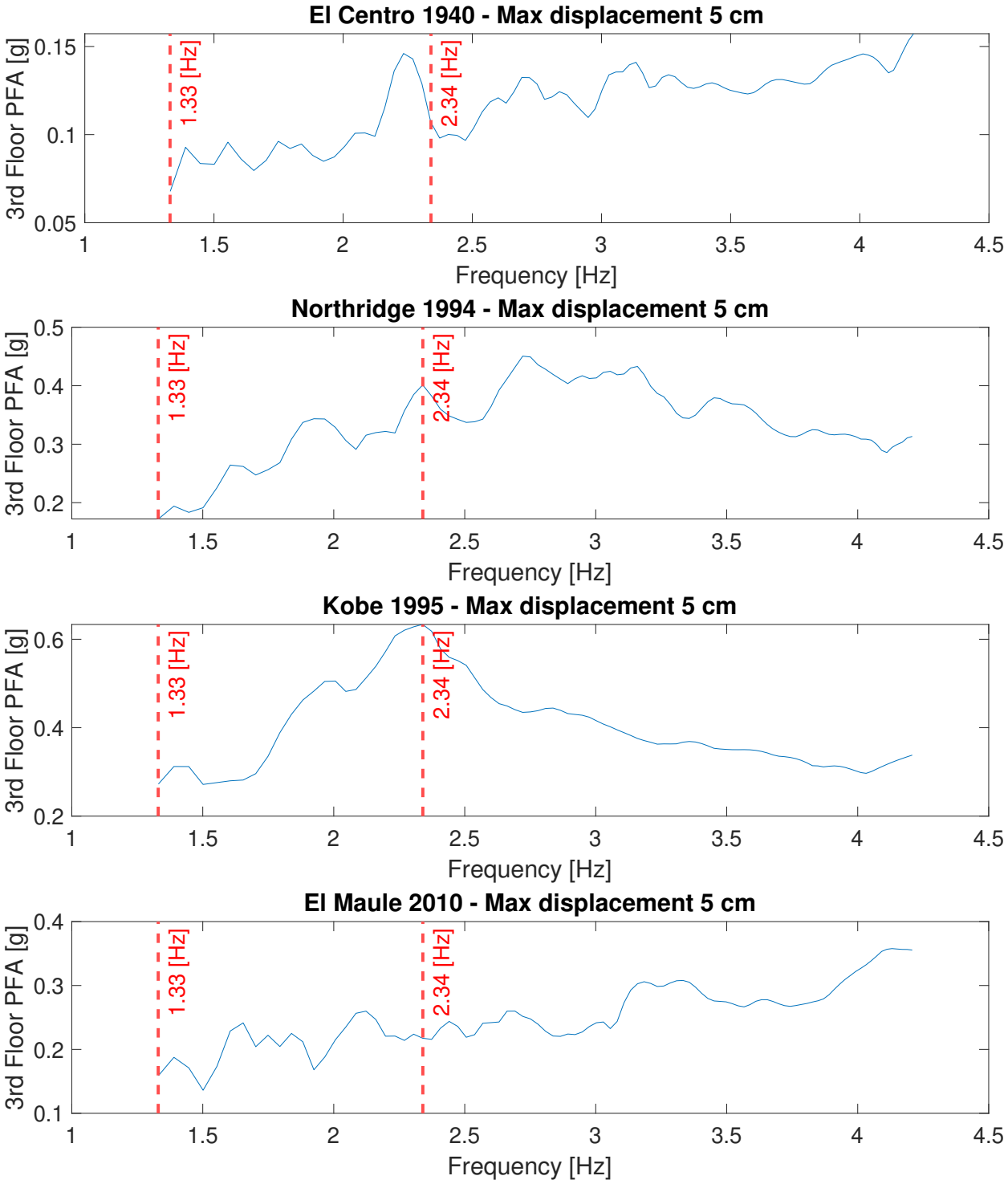

Figure 3.3: Maximum 3rd floor acceleration with different natural frequencies.

The parameters of the structure are adjusted to have a natural frequency of 2.34 [Hz] to achieve the largest possible PFA on the third floor, corresponding to Kobe's ground motion ($\beta = 3.1$). The

corresponding M, C (damping matrix is recalculated to maintain 1% Rayleigh damping fixed to the last two modes), and K matrices of the structure are shown in equations 3.10, 3.11, and 3.9, respectively.

$$[M] = \begin{bmatrix} 54.5 & 0 & 0 \\ 0 & 54.5 & 0 \\ 0 & 0 & 47.5 \end{bmatrix} [\text{kg}] \tag{3.9}$$

$$[C] = \begin{bmatrix} 50.3 & -13.0 & 0 \\ -13.0 & 55.2 & -13.6 \\ 0 & -13.6 & 38.5 \end{bmatrix} \left[\frac{\text{Ns}}{\text{m}}\right] \tag{3.10}$$

$$[K] = \begin{bmatrix} 118.6 & -71.1 & 0 \\ -71.1 & 145.0 & -74.0 \\ 0 & -74.0 & 74.0 \end{bmatrix} \left[\frac{\text{kN}}{\text{m}}\right] \tag{3.11}$$

The resulting structure has three natural frequencies with a damping ratio of 1.92% for the first natural frequency and 1% for the second and third natural frequencies (Table 3.1).

Table 3.1: Frequencies and damping ratios of the numerical substructure.

Frequency [hz]	damping ratio [%]
2.34	1.92
6.97	1.00
10.38	1.00

3.2.1 Numerical substructure

The numerical substructure consists of a three-story shear building with concentrated masses and 1% Rayleigh-type damping fixed to the last two modes. The equation of motion of the substructure is shown in Equation 3.12 where the M, C, and K matrices are the ones presented in equations 3.9, 3.10 and 3.11

$$\begin{bmatrix} \ddot{x}_1 \\ \ddot{x}_2 \\ \ddot{x}_3 \end{bmatrix} = -[M]^{-1}[K] \begin{bmatrix} x_1 \\ x_2 \\ x_3 \end{bmatrix} - [M]^{-1}[C] \begin{bmatrix} \dot{x}_1 \\ \dot{x}_2 \\ \dot{x}_3 \end{bmatrix} - [M]^{-1}\{\Gamma\}\ddot{x}_g - [M]^{-1} \begin{bmatrix} 0 \\ 0 \\ 1 \end{bmatrix} F_m \tag{3.12}$$

$$\Gamma = \begin{bmatrix} 1 \\ 1 \\ 1 \end{bmatrix} \tag{3.13}$$

The structure is modeled as a state-space system where the input vector is a two-dimensional vector containing the ground acceleration and the measured TMD's restitutive force (Equation 3.16). On the other hand, the state vector contains the relative displacements and velocities of the three structure's stories and the displacement and velocity of the ground, which is needed to obtain the absolute displacement of the third floor (Equation 3.15). The resultant state-space model is presented in Equation 3.14, where the system's output is the target displacement to be imposed by the shake table.

$$\begin{aligned} \{\dot{x}\} &= [A_s]\{x\} + [B_s]\{u\} \\ \{y\} &= [C_s]\{x\} + [D_s]\{u\} \end{aligned} \tag{3.14}$$

$$\{x\} = \begin{bmatrix} x_1 & x_2 & x_3 & \dot{x}_1 & \dot{x}_2 & \dot{x}_3 & x_g & \dot{x}_g \end{bmatrix}^T \tag{3.15}$$

$$\{u\} = \begin{bmatrix} \ddot{x}_g & F_m \end{bmatrix}^T \tag{3.16}$$

$$[A_s] = \begin{bmatrix} [0]_{3x3} & [I]_{3x3} & [0]_{3x2} \\ -[M]^{-1}[K] & -[M]^{-1}[C] & [0]_{3x2} \\ [0]_{2x3} & [0]_{2x3} & \begin{bmatrix} 0 & 1 \\ 0 & 0 \end{bmatrix} \end{bmatrix} \tag{3.17}$$

$$[B_s] = \begin{bmatrix} [0]_{3x1} & [0]_{3x1} \\ -[M]^{-1}\{\Gamma\} & -[M]^{-1}\begin{bmatrix} 0 \\ 0 \\ 1 \end{bmatrix} \\ [0]_{2x1} & \begin{bmatrix} 0 \\ 1 \end{bmatrix} \end{bmatrix} \tag{3.18}$$

$$[C_s] = \begin{bmatrix} 0 & 0 & 1 & 0 & 0 & 0 & 1 & 0 \end{bmatrix}, \quad [D_s] = \begin{bmatrix} 0 & 0 \end{bmatrix} \tag{3.19}$$

3.2.2 Experimental substructure

This experiment uses the same experimental setup as the one presented in the Subsection 2.2.3. However, both the masses and the springs that provide the restorative force have been modified to adjust to the fundamental frequency of the first mode of vibration of the structure; these properties

are shown in Table 3.2.

Table 3.2: TMD properties.

Property	Value
Mass [kg]	3.49
Stiffness [N/m]	756
Frequency [Hz]	2.33
Percentage of the building mass	2.24%

3.2.3 AMBC implementation

The shake table can be modeled in the Laplace domain as a function of the motor current I_m (Apkarian et al. 2017):

$$X(s) = \frac{1}{K_f s^2} I_m(s) \tag{3.20}$$

$$K_f = \frac{M_t P_b}{K_t} \tag{3.21}$$

where M_t is the total mass of the system (table plus payload); P_b is the pitch of the ball screw, and K_t is the motor current-toque constant

Also, the motor's current depends on the shake table's control law as shown in Equation 3.22.

$$I_m(s) = (K_p + sK_d)(X_d(s) - X(s)) \tag{3.22}$$

Replacing Equation 3.22 in Equation 3.20 we obtain

$$X(s) = \frac{K_p + sK_d}{K_f s^2 + K_p + sK_d} X_d(s) \tag{3.23}$$

which is the transfer function from the desired position to the position of the table.

The implemented shake table internal controller has a proportional gain $K_p = 10997.81$ and $K_d = 85.45$, which are fixed for this experiment. On the other hand, K_t, M_t, and P_b are parameters that depend on the physical properties of the system, and even when they have nominal values (Table 3.3), they still can be uncertain or change depending on the experiment.

Table 3.3: Shake table physical parameters (Quanser, 2017); (Danaher Motion, 2005).

Parameter	Value	Range
K_t	$0.36\ \left[\frac{Nm}{A}\right]$	[0.30,0.41]
P_b	$0.0063\ \left[\frac{m}{rev}\right]$	[0.006280,0.006320]
M_t	$23.63\ [kg]$	[7.7,30.83]

Note that the ranges presented in Table 3.3 depend on the shake table's physical parameters and the experiment's total mass. In the case of M_t, the range is defined by the minimum mass (table mass without payload) and the maximum payload to be tested. On the other hand, the range of P_b is defined based on the maximum allowable error for a ball screw class C5 (International Organization for Standardization, 2021), and for K_t a typical value of $\pm 10\%$ is assumed (Bouat, 2021).

In the particular case of this study the feedforward part of the AMBC considers only three states instead of the four proposed by Gálmez and Fermandois (2020): (i) target position , (ii) first derivative and, (iii) second derivative. This decision is to maintain the states related to physical quantities like displacement, velocity and acceleration and make the compensator easier to implement. However, the design and calibration process is the same as described in Subsection 3.1.1. The initial feedforward controller gains are set based on the feedforward compensator designed in Chapter 2, so if there is an improvement in the performance of the compensator, it is due to the adaptation process and not because the compensator has a better or worse starting point. To ensure robustness, the adaptive gains of the compensator (Equation 3.24) are set using the calibration process described in Subsection 3.1.1 with 200 offline realizations with random parameters. K_t and P_b parameters are selected using a normal distribution with a mean equal to the nominal value and a standard deviation equal to $\frac{\text{Range}}{6}$ so any possible value is between $\pm 3\sigma$ range; for M_t a uniform probability distribution is used.

$$\Gamma = \begin{bmatrix} \Gamma_1 \\ \Gamma_2 \\ \Gamma_3 \end{bmatrix} \tag{3.24}$$

The results from the 200 offline realizations are filtered to eliminate unstable responses, and the remaining are averaged and plotted (results with less than 50 stable realizations are discarded and plotted in white). To asses the performance of compensator on the calibration process three indicators are defined:

$$R_1 = \sum_{i=1}^{N} \frac{J_{1i}}{N} \tag{3.25}$$

$$R_2 = \sum_{i=1}^{N} \frac{J_{2i}}{N} \tag{3.26}$$

$$R_3 = \sum_{i=1}^{N} \frac{J_{3i}}{N} \tag{3.27}$$

The results presented in Figure 3.4 show that R_1 is relatively insensitive to the selection of the adaptive gains with a slight increase with $\Gamma_3 > 10^{3.5}$ and $\Gamma_2 < 10^{3.5}$ pairs. On the other hand, Figures 3.5 and 3.6 show that R_2 and R_3 have a slight dependence with Γ_1 and a higher dependence rate with Γ_2 and Γ_3. Furthermore, R_2 and R_3 values improve as Γ_2 and Γ_3 augments, however, the number of unstable realizations also augments, as shown in Figure 3.7.

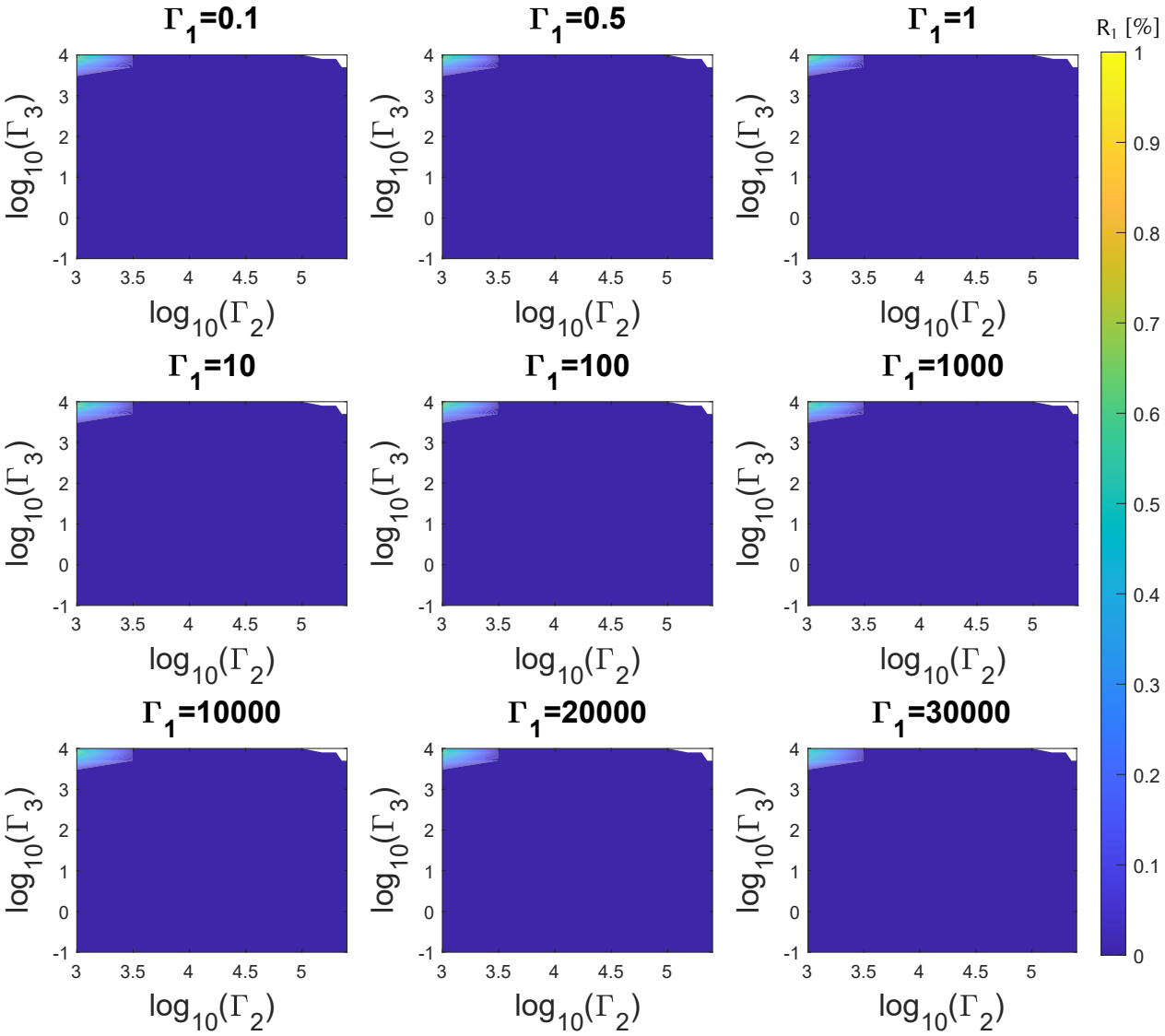

Figure 3.4: R_1 error indicator versus adaptive gains based on simulated data.

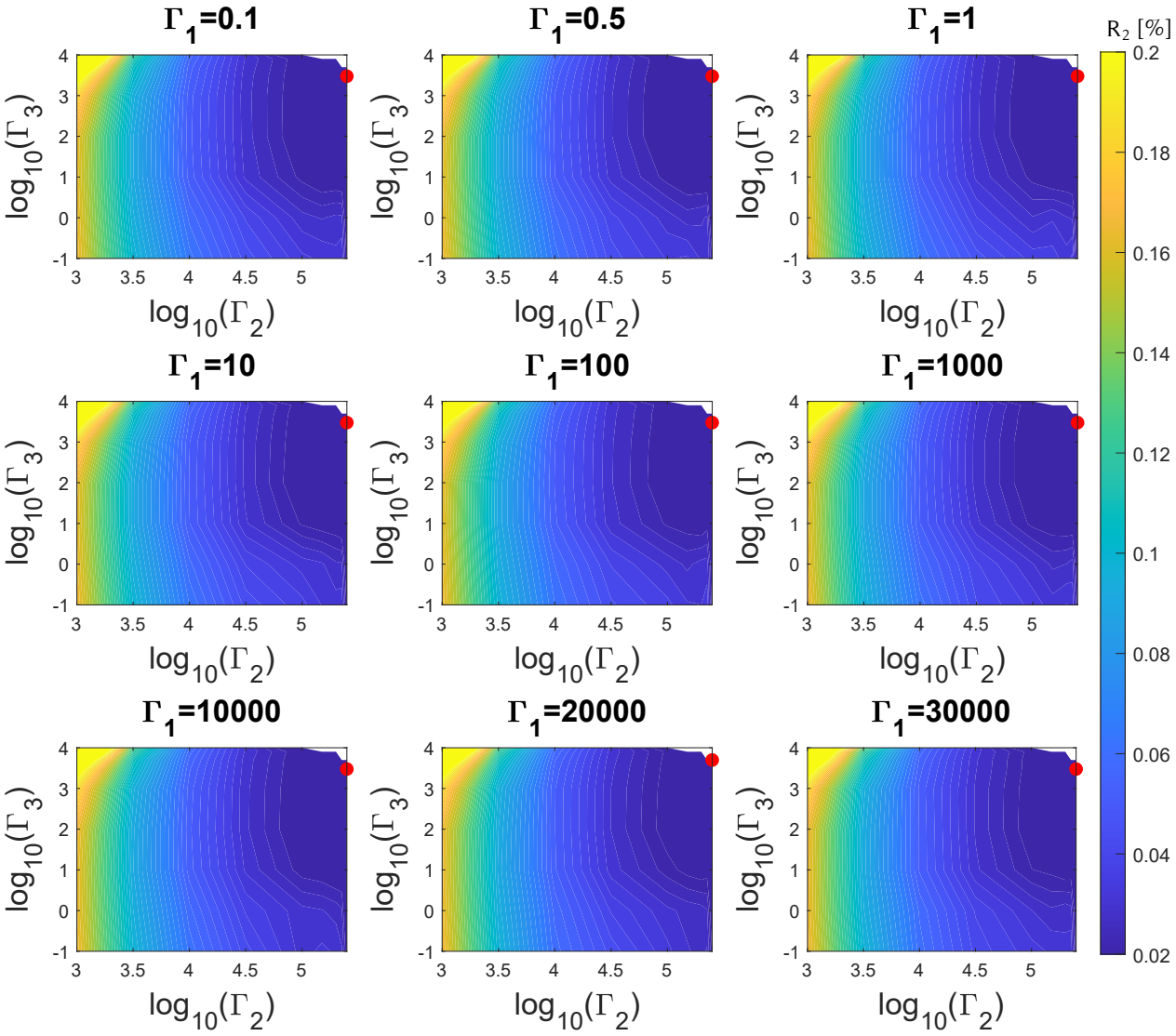

Figure 3.5: R_2 error indicator versus adaptive gains based on simulated data, red circle shows the minimum value.

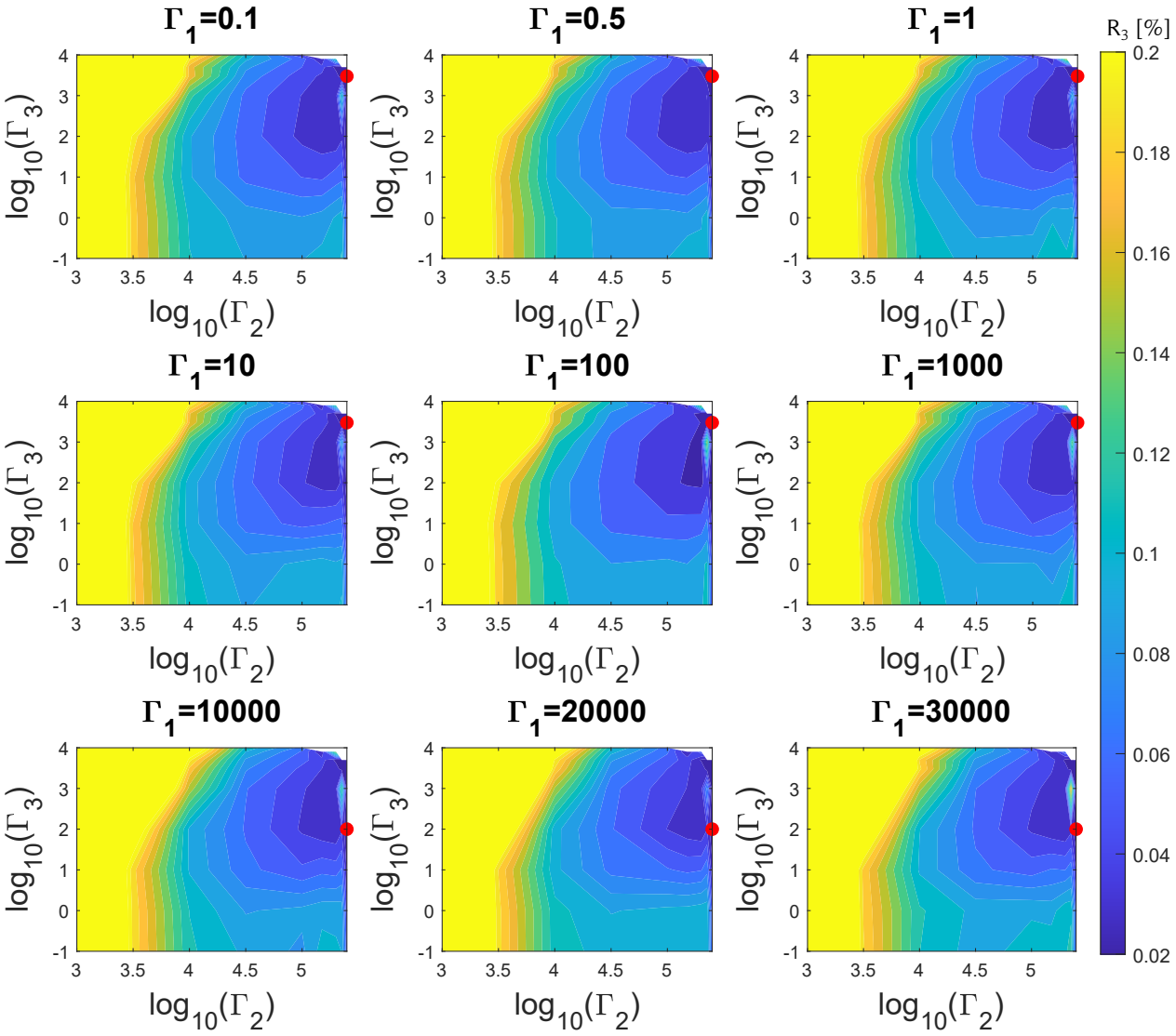

Figure 3.6: R_3 error indicator versus adaptive gains based on simulated data, red circle shows the minimum value.

It is important to notice that selecting the optimal parameters that minimize error can lead the system to zones with multiple unstable simulations (Figure 3.7). To ensure robustness, a trade-off between performance and stability is needed. Therefore, to include stability in the decision the cost function is defined as:

$$P(\Gamma) = 0.1\frac{R_1}{0.002} + 0.45R_2 + 0.45R_3 + 1.0\frac{200 - \text{N° of Stable Sims}}{200} \tag{3.28}$$

The R_1 indicator is normalized by 0.002 based on the observed values and the number of stable simulations is normalized by the total number of realizations per Γ. Additionally, the performance indicators are weighted based on desired performance. In this case the objective was to design a

robust compensator so the number of stable simulations is weighted by 1. On the other hand, R_1, R_2 and R_3 have a weight of 0.1, 0.45 and 0.45 respectively, to mainly reduce the tracking and peak error. Note that for this study the optimization process is performed after simulation of the entire optimization space which can be computationally intensive. However, this is not necessary and the optimization space can be efficiently explored using optimization algorithms if the cost function is defined previously.

Results presented in Figure 3.8 show that the optimal point is very close where the simulation starts to show unstable realizations. To avoid possible unstable results the adaptive gains is selected in a sub optimal point with similar $P(\Gamma)$ but further form the zone of unstable realizations. Finally, the selected value of Γ is $[\ 100 \quad 100000 \quad 100\ ]^T$.

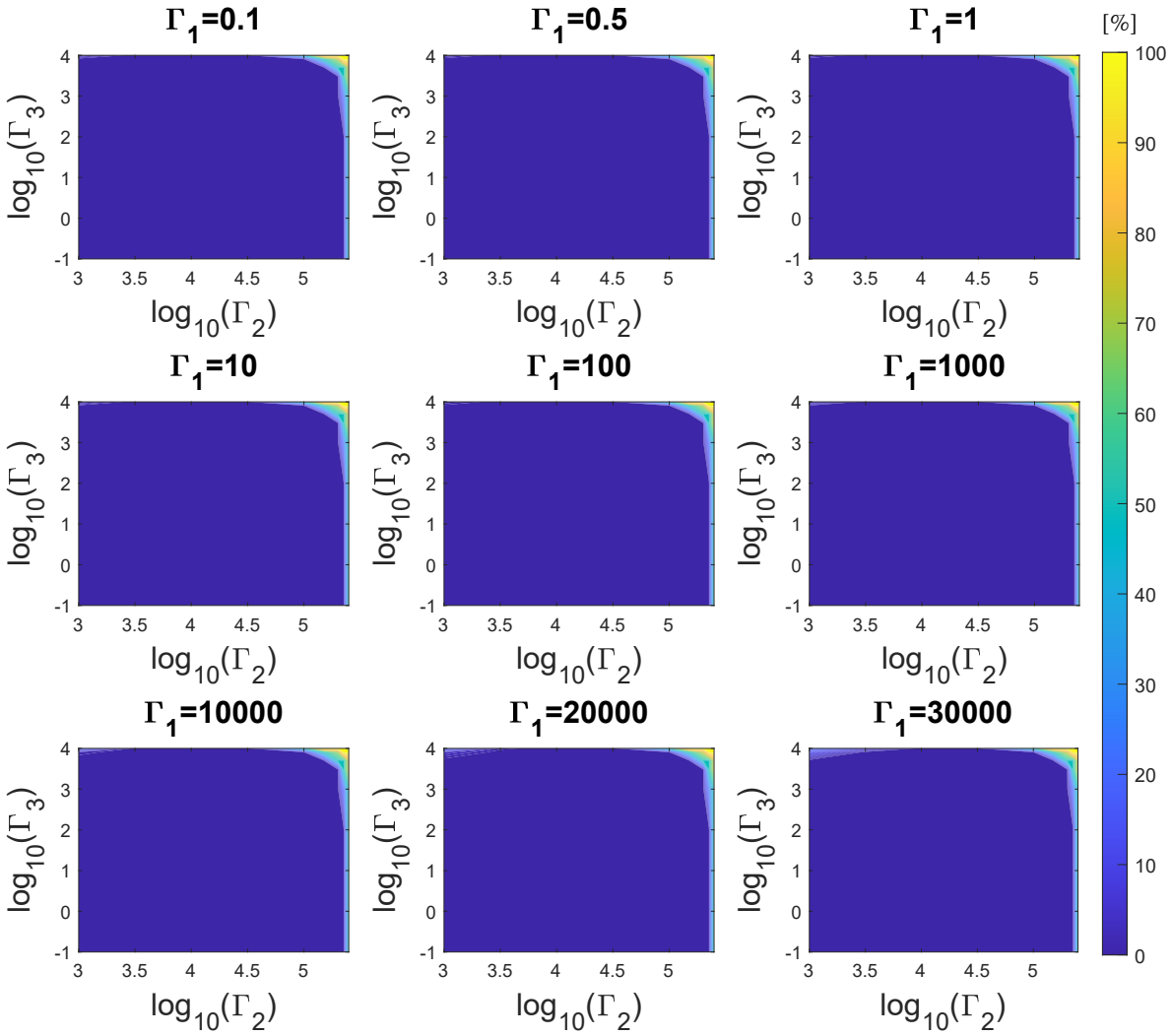

Figure 3.7: Percentage of unstable simulations versus adaptive gains based on simulated data.

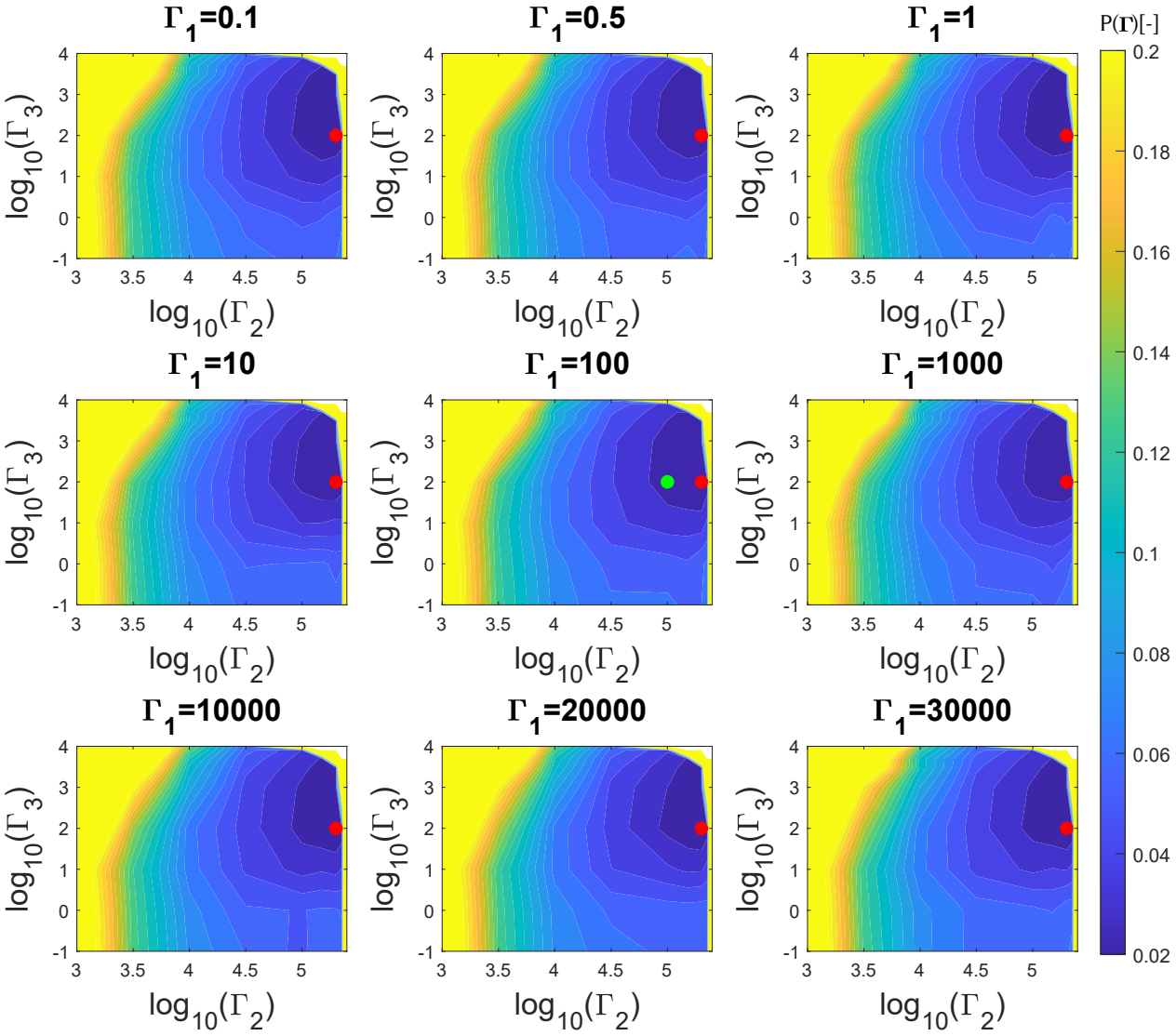

Figure 3.8: Cost function $P(\Gamma)$ versus adaptive gains based on simulated data, red circle shows the minimum value per Γ_3 and green circle shows the selected adaptive gains.

3.2.4 Test protocol

Three tests are proposed to test the performance of the AMBC:

- **Frame additional mass**: The objective is to address the performance of the AMBC versus a feedforward compensator when adding a payload to the shake table to modify the system's transfer function. The configurations are shown in Table 3.4.

Table 3.4: Additional reaction frame mass configurations.

Configuration name	Additional mass [kg]	Total mass [kg]	Theoretical peak acceleration [g]†
F0	0	23.63	0.82
F1	4.4	27.83	0.70
F2	7.2	30.83	0.63

†: This value is calculated based in the maximum rated acceleration of 2.5 [g] with 7.74 [kg] of payload.

The masses are added to the reaction frame symmetrical to TMD zero position to avoid generating torque and undesired vibrations. Figure 3.9 shows a picture of the experimental setup with additional mass. The ground motions used to this test are described in Table 3.5, these ground motions have been scaled accordingly with the optimization process described in section 3.2

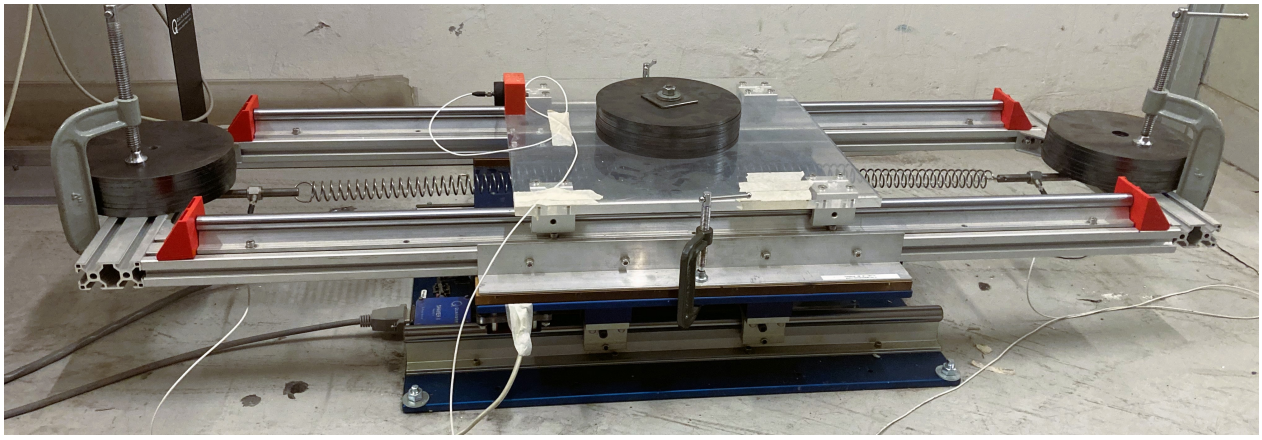

Figure 3.9: Additional mass is positioned on the end of the frame with a symmetrical distribution on each side.

Table 3.5: Ground motions used for the experiment.

Ground Motion	Station	Scale Factor	Test duration [s]
El Centro 1979 (Imperial Valley)	El Centro	10%	70
Northridge 1994	Sylmar Olive View Med FF	27%	70
Kobe 1995	HIK	120%†	170
Maule 2010	Concepción	23%	200

†: Scale factor reduced from 140% to 120% because it is too close to the maximum acceleration of the shake table.

- **Scale Factor**: This test aims to study the compensator's performance when the system reaches its physical limits (maximum rated acceleration) and whether both compensators remain stable under this condition. Both compensators are tested in RTHS with Kobe ground motion and scale factors of 80%, 100%, 120%, 140% in combination with three additional payload configurations (Table 3.4) per scale factor. Table 3.6 shows the theoretical maximum acceleration to be commanded to the shake table.

Table 3.6: Theoretical maximum acceleration to be commanded to the shake table.

Scale factor	Theoretical PGA [g]
80%	0.35
100%	0.44
120%	0.53
140%	0.62

- **Repeatability**: The objective of this test is to check if the results are consistent with a minor standard deviation over J_1, J_2, and J_3 errors. This experiment consist of 30 tests (15 with AMBC and 15 with feedforward compensator) subjected to Kobe ground motion at 120% scale factor and no additional frame mass.

3.3 Results and analysis

3.3.1 Frame aditional mass

Based on the results presented in Figure 3.10, it can be seen that there is no significant effect on the delay due to the increase in the mass of the frame (it is worth noticing that the minimum addressable delay is 1 [ms] due to the sample rate). Moreover, the performance of the AMBC is better than the feedforward in all the tested scenarios, with a difference between 1 to 3 [ms] of average delay.

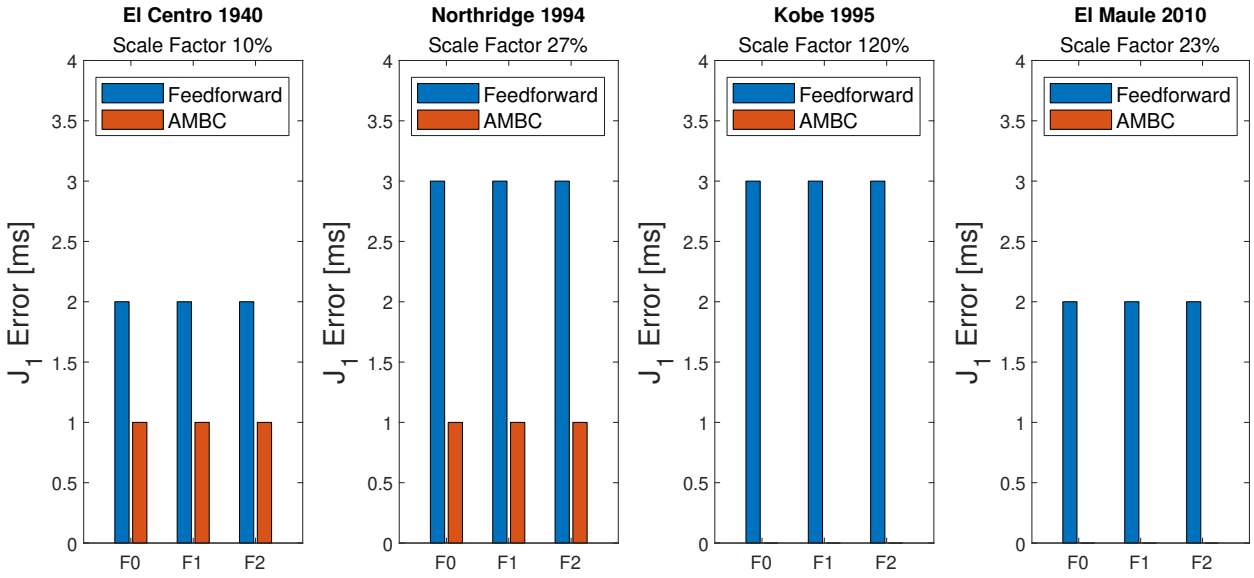

Figure 3.10: Impact of the external mass on J_1 error with different ground motions.

The results presented in Figure 3.11 and Figure 3.12 for J_2 and J_3 errors show that both compensators have good results with worst performance for Kobe. This higher error is attributable to the fact that Kobe is the earthquake with the highest PGA of the four, placing greater demands on the shake table and reaching the limits of its capability. However, the performance of the AMBC is equal or better in all tested scenarios with improvements between 0.1% to 1% of the RMS error and 0% to 2% on peak error.

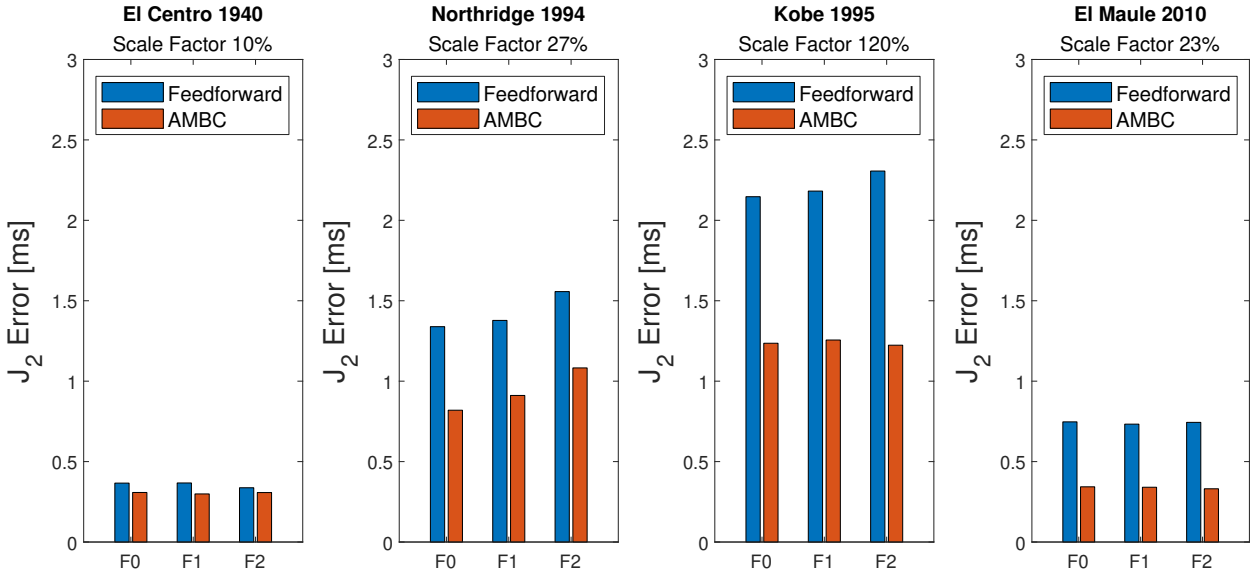

Figure 3.11: Impact of the external mass on J_2 error with different ground motions.

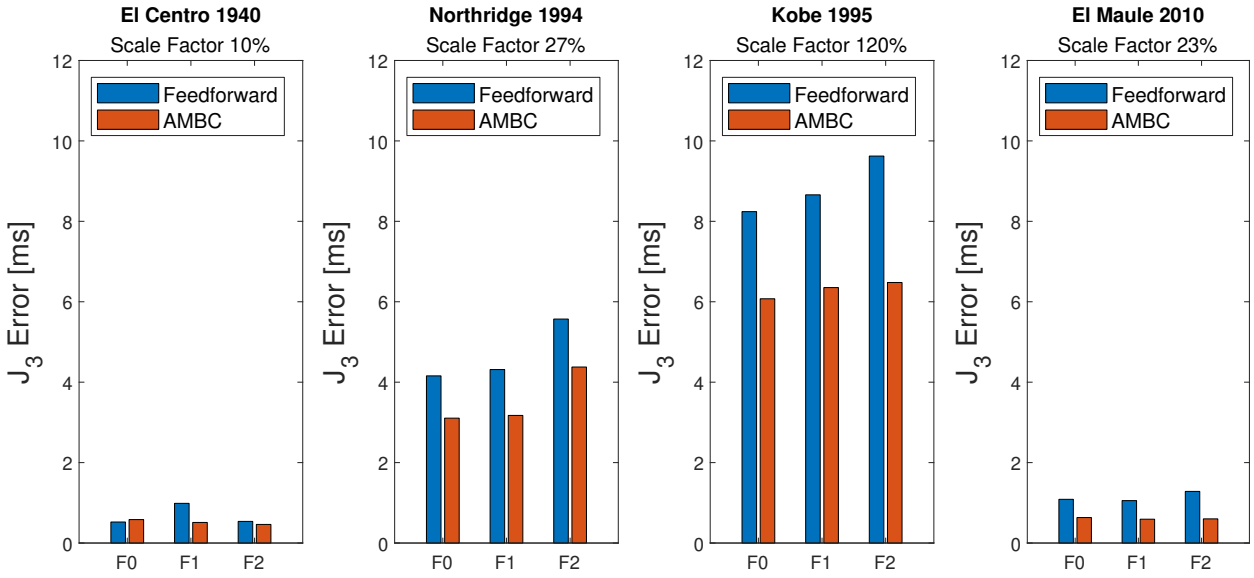

Figure 3.12: Impact of the external mass on J_3 error with different ground motions.

3.3.2 Scale factor

The tests performed increasing the scale factor of the Kobe seismic record (Figure 3.13) show that for the feedforward compensator, there is an increase of the delay with higher demands with no effect of the external mass. In the AMBC case, there is no increase in delay with sub 1 [ms] average delay for all scale factors and mass combinations. On the other hand, J_2 and J_3 show an increase in the error with the scale factor for both compensators with little dependence on the external mass. However, the performance of the AMBC is better than that of the feedforwards in all tested scenarios. It is worth mentioning that the AMBC remains stable even with errors as high as 20%.

The frequency domain response presented in Figure 3.14 shows that both compensators have similar magnitudes but different phases. The slope of the phase can be correlated proportionally to delay, and results show that for the feedforward compensator, the delay augments with the scale factor supporting the results obtained for J_1. On the other hand, the AMBC shows an almost constant phase value for the cases of 80%, 100%, and 120%. However, in the case of 140%, the AMBC exhibits a slightly positive slope, which indicates overcompensation. This overcompensation is probably produced by too aggressive control parameters when trying to overcome the physical limitations of the actuator. The physical limitations of the shake table were not modeled, and they will require a more complex model to be included in the calibration phase of the AMBC. Besides, even when this result for the 140% case is not optimal, the system remains stable with better performance than the feedforward compensator. Note that the results are only presented between 0-2 [Hz], which is

the predominant frequency content of the target displacement, details are shown in the appendix (Figure 4.1).

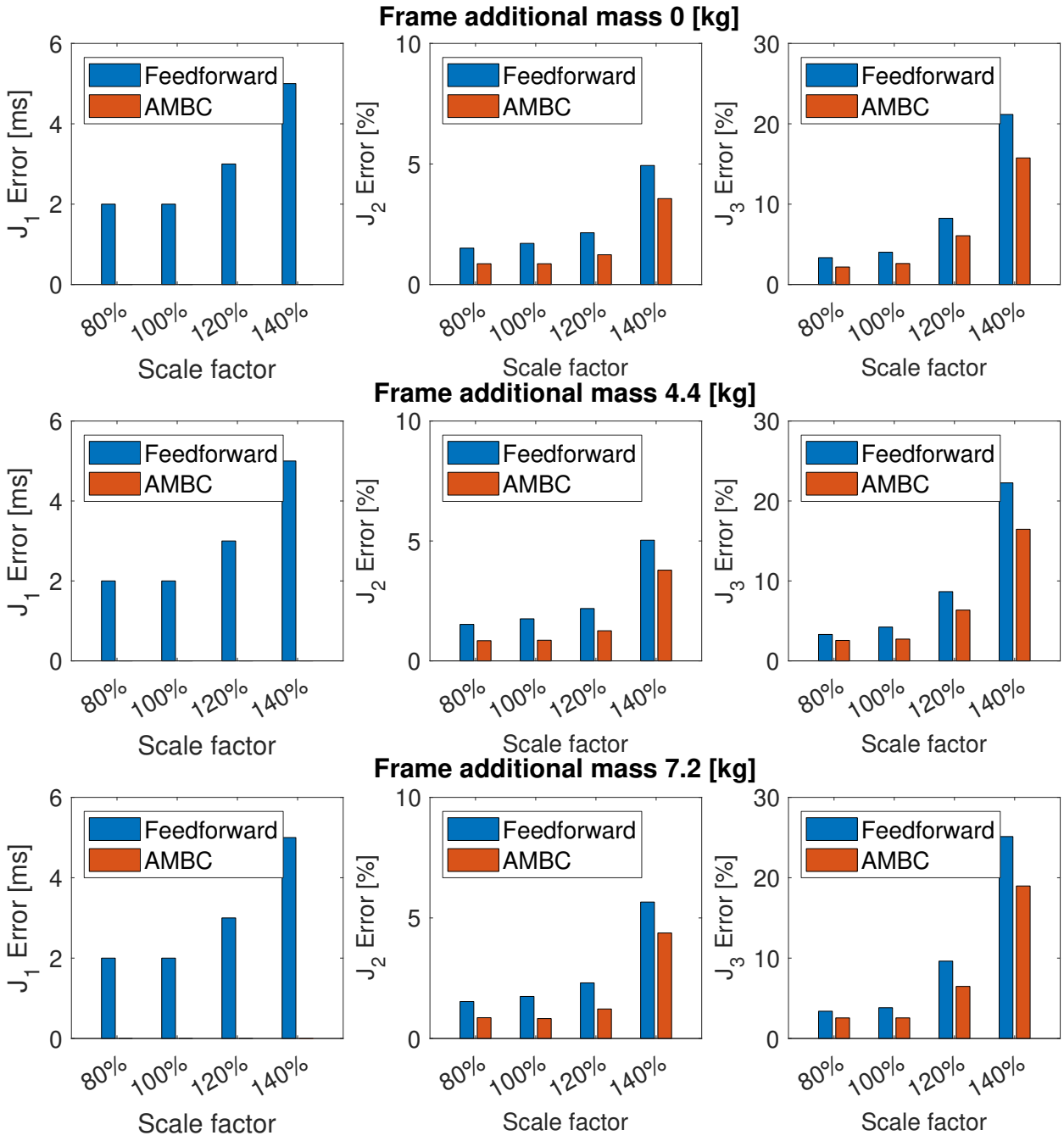

Figure 3.13: Effect of the scale factor on J_1, J_2 and J_3 errors for a 3 story building with TMD subjected to Kobe earthquake.

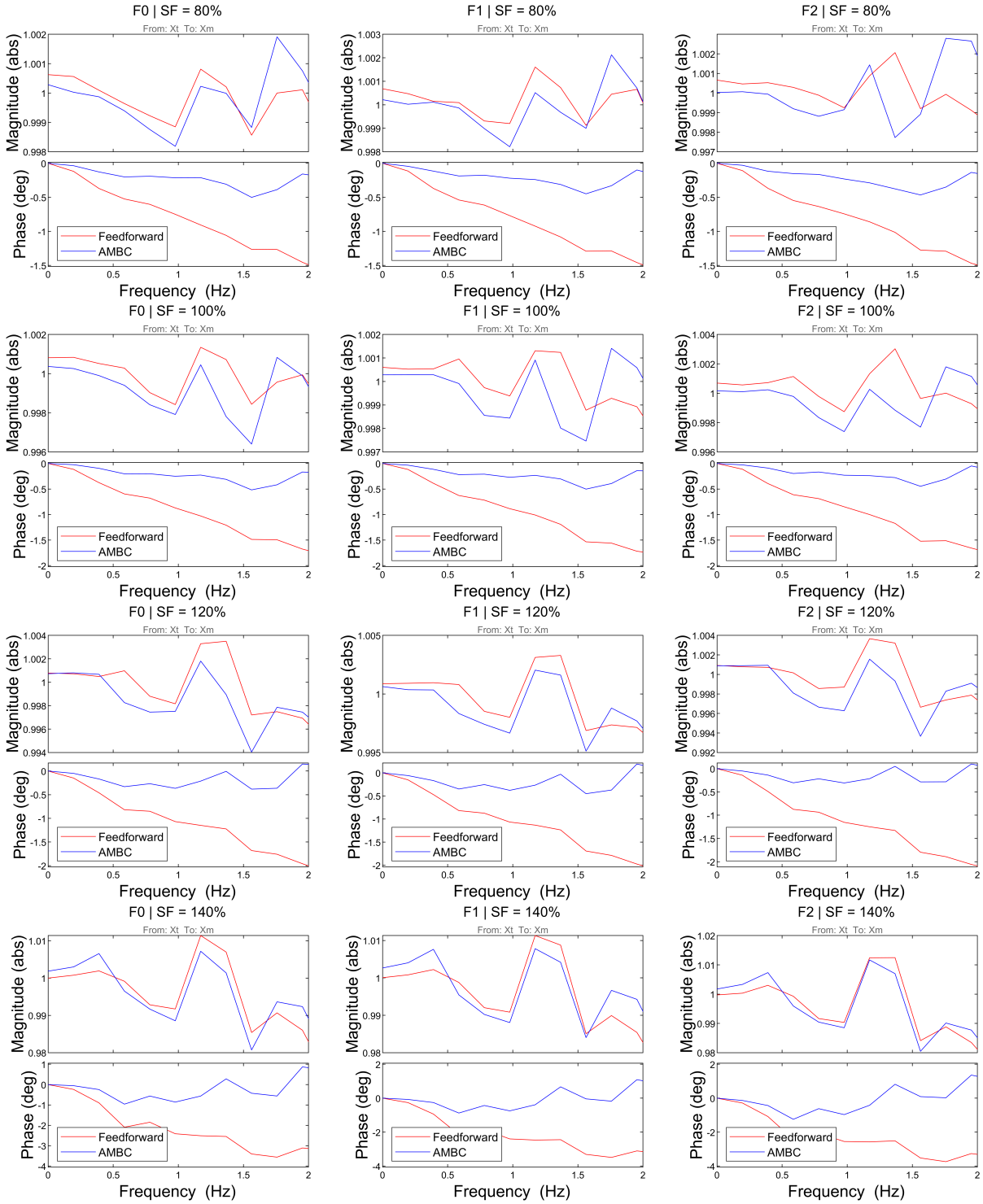

Figure 3.14: H_2 estimator of the frequency response function between target and measured displacement.

3.3.3 Repeatability

The obtained results exhibit a slight standard deviation for J_1 and J_2 errors with a mean delay of 3 [ms] and 2.2% RMS error for the feedforward compensator, and less than 1 [ms] with 1.2% RMS error for the AMBC case. On the other hand, the J_3 error shows a maximum relative error of 8.8% for the feedforward compensator and 5.8% with the AMBC; both compensators show similar standard deviations. The small standard deviation relative to the mean value supports the results obtained in Subsection 3.3.1 and Subsection 3.3.2 and shows that the performance improvement is consistent and not an outlier.

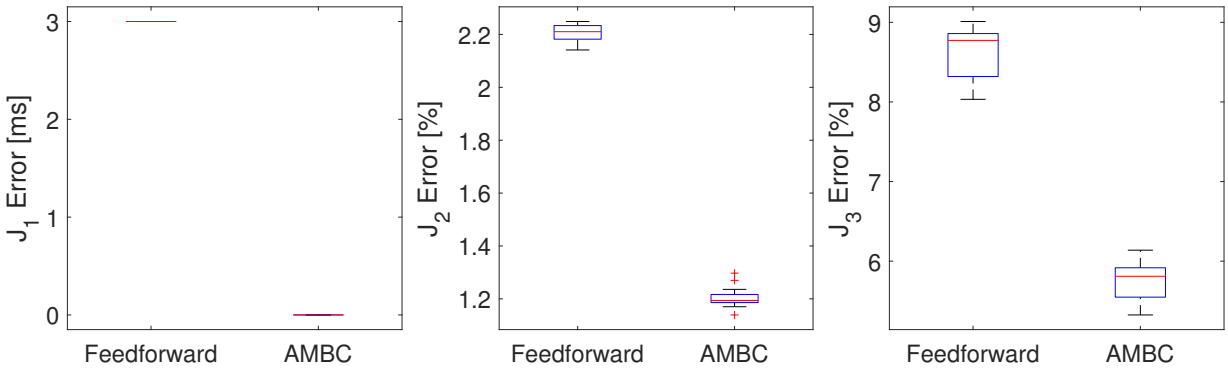

Figure 3.15: J1, J2 and J3 mean error for both compensators (15 tests per compensator).

The adaptive parameters shown in Figure 3.16 displays a consistent behavior of the parameters with low variability between experiments. Also, the parameters shows that the compensator adapt the parameters during the seismic motion (first 140 seconds) and they tend to a constant value in the free vibration phase which is the expected behavior.

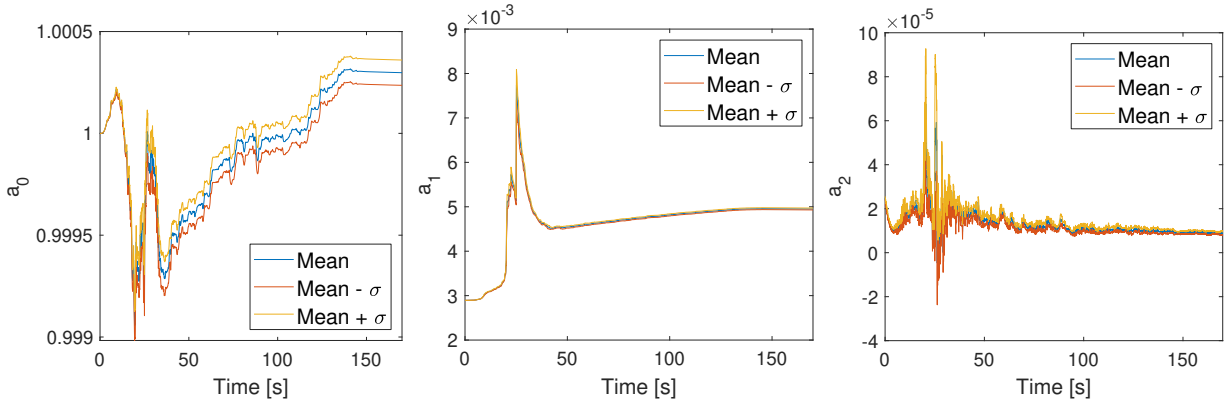

Figure 3.16: Mean of the adaptive parameters over time.

Figure 3.14 shows the average frequency response function between target to measured position, the results show similar behavior in terms of magnitude with values around the unity gain. On the other side, feedforward's phase shows a negative slope and the AMBC an almost constant value similar to the results presented in Subsection 3.3.2.

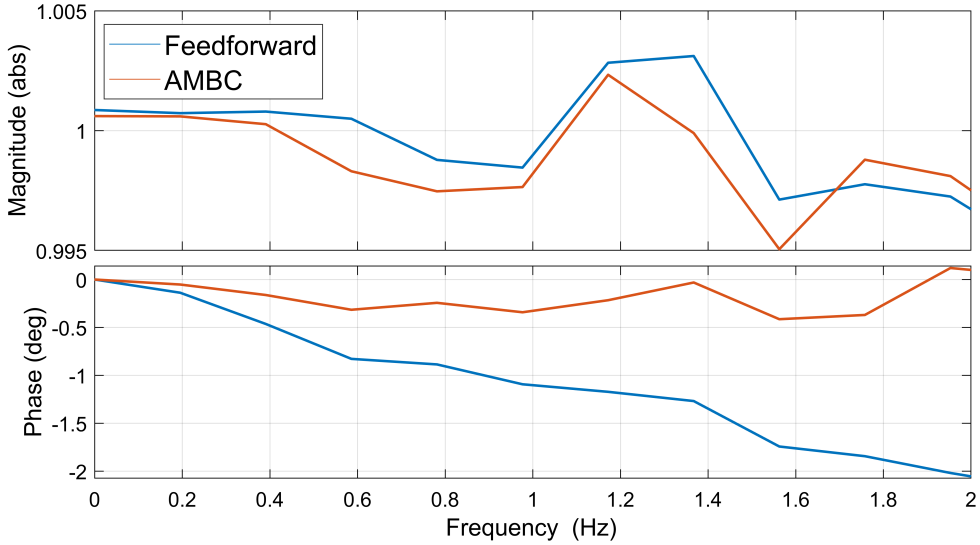

Figure 3.17: Average of the frequency response function from target to measured position.

3.4 Summary

To address the AMBC performance in different scenarios, three RTHS of a three story building equipped with a TMD were conducted and compared against a feedforward compensator. In the first test, additional payload was added to the actuator to modify the transfer function of the system without modifying the dynamics of the TMD. In a second experiment, the scale factor of the input was varied between 80% and 100% of the Kobe 1995 earthquake keeping a fixed control plant. Finally, the last experiment consist in 15 tests per compensator with fixed parameters to analyze the consistency of the results.

The experiments used to test the performance of the AMBC show that in all cases, the AMBC has equal or better performance than the feedforward compensator. This improvement in the performance is up to 6 [ms] on J_1, 1.3 % on J_2, and 6 % on J_3. In all cases the AMBC was stable with residuals that tend to zero, showing a good robustness of the compensator. In the case of Kobe with a scale factor of 140%, the results show that the AMBC exhibits better performance in terms all three error metrics with a slight overcompensation shown as a positive phase slope in the

frequency response function. Also, Kobe results show higher J_2 and J_3 errors for both compensators, but this may be attributable to the fact that the shake table is reaching its physical limitations. Nevertheless, the AMBC maintains sub 1 [ms] of average delay when the feedforward compensator shows deterioration up to 6 [ms] as the demand increases. It is worth noticing that even when the improvement in the performance is not substantial, designing the feedforward compensator require the identification of the control plant. In contrast, the AMBC design process requires a model of the control plant and the implementation of a more complex algorithm with a calibration process that can be computationally intensive.

Chapter 4

Conclusions

4.1 Conclusions

To study the performance and robustness of the AMBC this research performed several RTHS tests of a three-story building equipped with a TMD in the Dynamics Laboratory of the Civil Engineering Department at Universidad Federico Santa María. First, the designed testbed and experimental framework are tested against a reference model of the structure equipped with the TMD and subjected to four ground motions to validate the methodology. The results showed a good correlation with the reference model and a similar response in terms of maximum amplitude and time response. On the other hand, the subspace synchronization plots show a good correlation between measured and target signals. Furthermore, the error indicators exhibit a delay of 2 [ms] and a tracking and peak error of less than 2%. These results lead to the conclusion that the experimental framework and test bed works as intended and can be used to benchmark the AMBC.

To benchmark the AMBC, 3 series of RTHS tests were carried out, analyzing the uncertainty of the control plant, the effect of the magnitude of the demand on the actuator, and the repeatability of the results. The experiments showed that the compensator outperformed the feedforward compensator in all tested scenarios with improvements in delay, tracking, and peak error. The observed improvements in delay were up to 6 [ms] in scenarios where the scale factor of the ground motion is higher and the actuator is pushed to the limits of its capabilities, which indicates that the AMBC adapts well to the change in the dynamics even in challenging scenarios. Furthermore, the tracking and peak errors show a slight improvement with an average of 1% and a maximum of 6% in cases of higher actuator demands with no stability issues. Additionally, in the repeatability experiment the RTHS consistently outperforms the feedforward compensator with lower delay, and smaller tracking and peak errors. The adaptive parameters also show a consistent behavior with similar values across all realizations which indicates that noise present in the experiment is not severely affecting the adaptation process. Moreover, the frequency response functions of both compensators exhibit similar magnitudes around the unity gain and almost zero phase in the case of the AMBC which supports the lower delay observed in the other experiments. Based on all the obtained results, the AMBC adequately compensates the actuator dynamics and shows good adaptation to the changes in the control plant without losing robustness.

4.2 Future work

Based on the results of the experimental tests there is evidence that the compensator works as intended with a low delay and small tracking error. Therefore, the next step is to address the

compensator's performance in more challenging scenarios like nonlinear control plants. The experimental setup presented in this study can be slightly modified to install a nonlinear springs or a nonlinear compliant mechanism. Another alternative is to provide the system a nonlinear dampening device or a controllable device like a magneto-rheological damper.

On the other hand, it is essential to ensure stability in extreme cases like slipping, crashing, or fragile behavior where the change in the control plant is sudden, in which too aggressive adaptive parameters can make the compensator unstable, and less aggressive adaptive parameters can result in sub-optimal compensation. These cases can be simulated and added to the uncertainty considered in the calibration process and later on experimentally tested to validate the virtual results.

References

Apkarian, J., Lévis, M., & Molki, A. (2017). *Laboratory Guide, Shake Table II* (tech. rep.). Quanser.

Bouat, M. (2021). *Physical parameters affecting stall torque of a brushless motor* (tech. rep.). Portescap.

Carrion, J. E., Spencer, B. F., & Phillips, B. M. (2010). Real-time hybrid simulation for structural control performance assessment. *Earthquake Engineering and Engineering Vibration 2009 8:4*, *8*, 481–492. https://doi.org/10.1007/S11803-009-9122-4

Carrion, J. E., Spencer, B. F., Elnashai, A. S., Alleyne, A. G., & Hajjar, J. F. (2007). *Model-based strategies for real-time hybrid testing.*

Chae, Y., Kazemibidokhti, K., & Ricles, J. M. (2013). Adaptive time series compensator for delay compensation of servo-hydraulic actuator systems for real-time hybrid simulation. *Earthquake Engineering & Structural Dynamics*, *42*, 1697–1715. https://doi.org/10.1002/EQE.2294

Chen, C., & Ricles, J. M. (2010). Tracking error-based servohydraulic actuator adaptive compensation for real-time hybrid simulation. *Journal of structural engineering*, *136*(4), 432–440.

Chen, P. C., Chang, C. M., Spencer, B. F., & Tsai, K. C. (2015). Adaptive model-based tracking control for real-time hybrid simulation. *Bulletin of Earthquake Engineering*, *13*, 1633–1653.

Connor, J. J. (2003). *Structural motion control.* Pearson Education, Inc New York, NY, USA.

Danaher Motion. (2005). *AKM series motors* (tech. rep.). Danaher Motion.

Dermitzakis, S., & Mahin, S. (1985). *Development of substructuring techniques for on-line computer controlled seismic performance testing.* Earthquake Engineering Research Center, College of Engineering, University of California. https://books.google.cl/books?id=hiwIAQAAIAAJ

dSpace. (2020). *dSpace MicroLabBox III, Datasheet* (tech. rep.). dSpace. https://www.dspace.com/shared/data/pdf/2020/dSPACE-MicroLabBox_Product-Brochure_2020-01_EN.pdf

Dyke, S. J., SpencerJr., B. F., Quast, P., & Sain, M. K. (1995). Role of control-structure interaction in protective system design. *Journal of Engineering Mechanics*, *121*, 322–338. https://doi.org/10.1061/(ASCE)0733-9399(1995)121:2(322)

Fermandois, G. A., Galmez, C., & Valdebenito, M. (2020). Optimal gain calibration of adaptive model-based compensation for real-time hybrid simulation. In 17WCEE (Ed.). 17WCEE. https://www.researchgate.net/publication/344115325

Frahm, H. (1909). *Device for damping vibration of bodies.* (No. 989,958).

Gálmez, C., & Fermandois, G. (2020). Online stability analysis for real-time hybrid simulation testing. *Frontiers in Built Environment*, *6*. https://doi.org/10.3389/FBUIL.2020.00134/FULL

Hakuno, M., Shidawara, M., & Hara, T. (1969). Dynamic destructive test of a cantilever beam, controlled by an analog-computer. *Proceedings of the Japan Society of Civil Engineers*, *1969*(171), 1–9. https://doi.org/10.2208/jscej1969.1969.171_1

Horiuchi, T. (1996). Development of a real-time byberid experimental system with actuator delay compensation. *Proc. 11th World Conf. Earthquake Eng. Acapulco, Mexico*, *660*.

Horiuchi, T., Inoue, M., Konno, T., & Namita, Y. (1999). *Real-time hybrid experimental system with actuator delay compensation and its application to a piping system with energy absorber.*

International Organization for Standardization. (2021). *Part 2: Nominal diameters, leads, nut dimensions and mounting bolts* (Standard). International Organization for Standardization. Geneva, CH.

Kaba, S., & Mahin, S. (1984). *Refined modelling of reinforced concrete columns for seismic analysis.* University of California, Earthquake Engineering Research Center. https://books.google.cl/books?id=cygIAQAAIAAJ

Kim, S. B., Spencer, J. F., & Yun, C. B. (2005). Frequency domain identification of multi-input, multi-output systems considering physical relationships between measured variables. *Journal of Engineering Mechanics*. https://doi.org/10.1061/(ASCE)0733-9399(2005)131:5(461)

Li, N., Tang, J., Li, Z.-X., & Gao, X. (2022). Reinforcement learning control method for real-time hybrid simulation based on deep deterministic policy gradient algorithm. *Structural Control and Health Monitoring*, *29*(10), e3035.

Melchers, R. E., & Beck, A. T. (2018). *Structural reliability analysis and prediction.* John wiley & sons.

Nakashima, M., Kato, H., & Takaoka, E. (1992). Development of real-time pseudo dynamic testing. *Earthquake Engineering & Structural Dynamics*, *21*, 79–92. https://doi.org/10.1002/EQE.4290210106

Ormondroyd, J., & Den Hartog, J. (1928). The theory of the dynamic vibration absorber. *Journal of Fluids Engineering*, *49*(2).

Palacio-Betancur, A., & Soto, M. G. (2019). Adaptive tracking control for real-time hybrid simulation of structures subjected to seismic loading. *Mechanical Systems and Signal Processing*, *134*, 106345.

PCB Electronics. (2016). *ICP Force Sensor Model 208C05, Datasheet* (tech. rep.). PCB Electronics. https://www.pcb.com/products?m=208c05

Phillips, B. M., & Spencer, B. F. (2011). Model-based feedforward-feedback tracking control for real-time hybrid simulation. *Newmark Structural Engineering Laboratory Report Series 028*.

Phillips, B. M., & Spencer, B. F. (2013). Model-based feedforward-feedback actuator control for real-time hybrid simulation. *Journal of Structural Engineering*, *139*, 1205–1214. https://doi.org/10.1061/(ASCE)ST.1943-541X.0000606

Quanser. (2017). *User Manual, Shake Table II, Set Up and Configuration* (tech. rep.). Quanser.

Randall, S., Halsted III, D., & Taylor, D. (1981). Optimum vibration absorbers for linear damped systems.

Saouma, V., & Sivaselvan, M. (2008). *Hybrid simulation: Theory, implementation and applications* (V. Saouma & M. Sivaselvan, Eds.). CRC Press. https://doi.org/10.1201/9781482288612

Silva, C. E., Gomez, D., Maghareh, A., Dyke, S. J., & Spencer, B. F. (2020). Benchmark control problem for real-time hybrid simulation. *Mechanical Systems and Signal Processing*, *135*, 106381. https://doi.org/10.1016/J.YMSSP.2019.106381

Takanashi, K., Udagawa, K., Seki, M., Okada, T., & Tanaka, H. (1975). Non-linear earthquake response analysis of by a computer-actuator on-line system. *Transactions of the Architectural Institute of Japan*, *229*, 77–83, 190. https://doi.org/10.3130/AIJSAXX.229.0_77

Tao, J., & Mercan, O. (2019). A study on a benchmark control problem for real-time hybrid simulation with a tracking error-based adaptive compensator combined with a supplementary proportional-integral-derivative controller. *Mechanical Systems and Signal Processing*, *134*, 106346.

Tsai, H.-C., & Lin, G.-C. (1993). Optimum tuned-mass dampers for minimizing steady-state response of support-excited and damped systems. *Earthquake engineering & structural dynamics*, *22*(11), 957–973.

Tsokanas, N., Pastorino, R., & Stojadinović, B. (2022). Adaptive model predictive control for actuation dynamics compensation in real-time hybrid simulation. *Mechanism and Machine Theory*, *172*, 104817.

Warburton, G. B. (1982). Optimum absorber parameters for various combinations of response and excitation parameters. *Earthquake Engineering & Structural Dynamics*, *10*(3), 381–401.

Xu, G., Ning, X., Huang, W., Wang, Z., & Zheng, L. (2023). A model-based adaptive control method for real-time hybrid simulation. *Smart Structures and Systems, An International Journal*, *31*(5), 437–454.

Appendix

A. Frequency content of target displacement

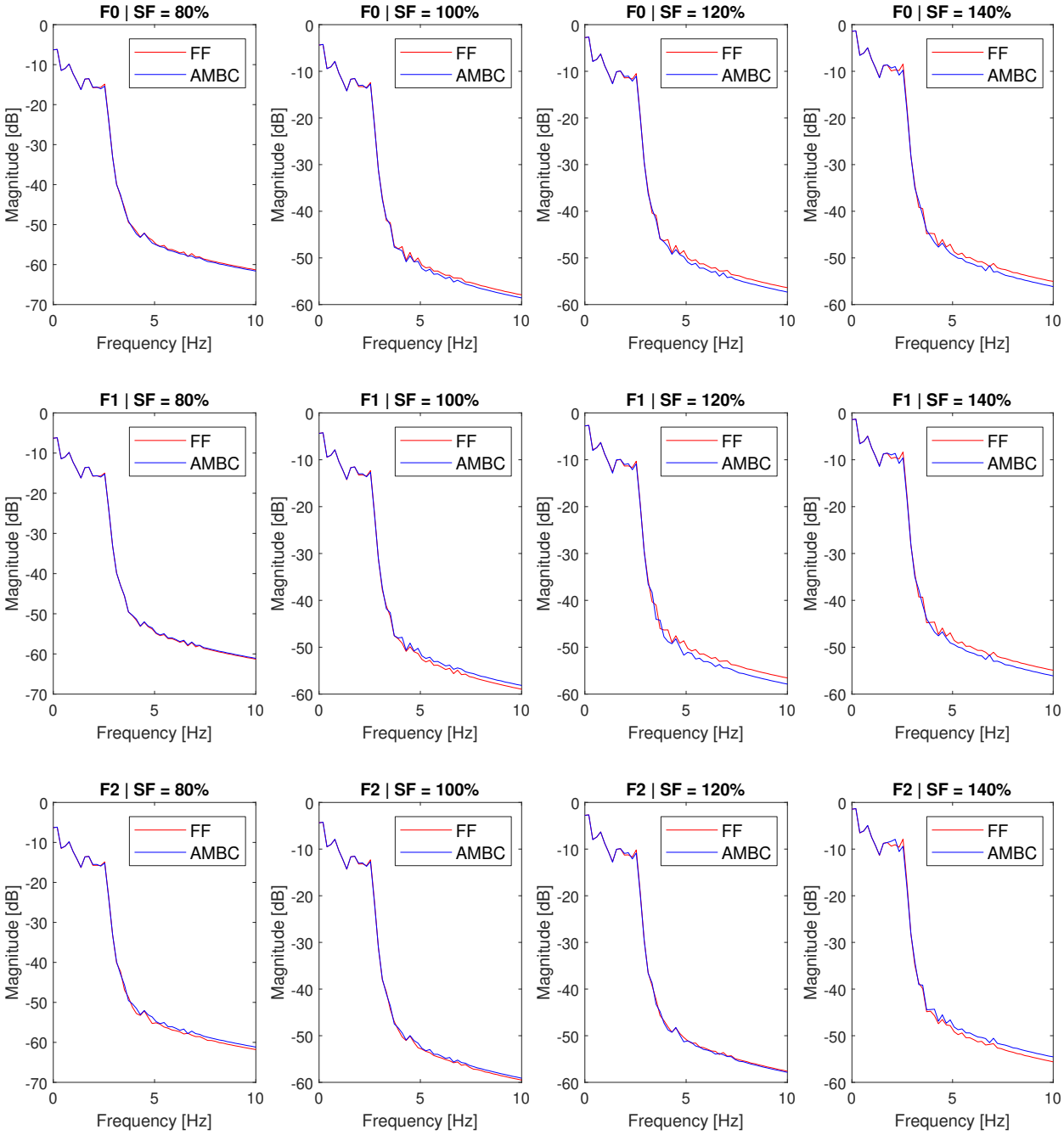

Figure 4.1: Frequency content of the target displacement for test of Subsection 3.3.2.